MATERIALS, TECHNOLOGIES, CONSTRUCTIONS

“Constructions and design”

Redakcja naukowa:
dr hab. inż. Aleksander Mazurkow, prof. PRz

Stalowa Wola 2019

Wydano za zgodą Rektora

O p i n i o d a w c y

dr hab. inż. Zenon Aleksander Opiekun, prof. PRz
dr hab. inż. Mirosław Tupaj, prof. PRz

R e d a k t o r n a c z e l n y

Wydawnictw Politechniki Rzeszowskiej
prof. dr hab. Grzegorz Ostasz

R e d a k t o r W y d a n i a

dr hab. inż. Aleksander Mazurkow, prof. PRz

O p r a c o w a n i e m a t r y c i o k ł a d k i

dr inż. Joanna Zielińska-Szwajka
mgr inż. Sylwia Sikorska-Czupryna

materials, technologies,
constructions, testing

ISBN 978-83-7934-359-1

Ark. wyd. 3,58, ark. druk. 4,25
Oficyna Wydawnicza Politechniki Rzeszowskiej
al. Powstańców Warszawy 12, 35-959 Rzeszów
https://oficyna.prz.edu.pl
Zam. nr 103/19

Table of Contents

Chapter 1.

Andrzej CHMIELOWIEC[1*]
Wojciech HOMIK[2]

MODELLING OF A TORSIONAL VIBRATIONS VISCOUS DAMPER USING THE HYDRODYNAMIC THEORY OF ROTATING ELEMENTS LUBRICATION

Abstract
Viscous dampers are one of the ways of reducing torsional vibrations in multi-cylinder internal combustion engine crankshafts. The damping element often used in this type of devices is a plunger immersed in silicone oil of very high viscosity. Until now the state of a damper has been modelled based on rather idealized assumptions and without any hydrodynamic analysis of the state of oil inside it. Unfortunately such models do not explain the reasons behind excessive and too fast wear of oil and the active surfaces of the damper. Searching for the causes of damper breakdowns, the authors decided to develop a new mathematical model based on the rotating elements lubrication theory. This paper explains the hydrodynamic modelling of a torsional vibrations viscous damper and discusses the problems that must be solved so that the model can be developed.

Keywords:
tribology, hydrodynamic modelling, lubrication theory, torsional vibrations, vibrations damping, viscous damper

1. Introduction
The second part of this paper outlines the issue of torsional vibrations occurring in combustion engines. Apart from a general characteristic of this problem, it also provides an insight into the methods used so far to model torsional vibration

[1] Faculty of Mechanics and Technology, Rzeszow University of Technology, al. Powstańców Warszawy 12, 35-959 Rzeszów, Poland
[2] Faculty of Mechanical Engineering and Aeronautics, Rzeszow University of Technology, al. Powstańców Warszawy 12, 35-959 Rzeszów, Poland
[*]e-mail: achmie@prz.edu.pl

dampers. The third part proposes to add hydrodynamic modelling of the effects that occur during the operation of the said dampers to the methods used so far. The initial numerical results allow us to suspect that this type of modelling may substantially contribute to this field of science.

2. Torsional vibrations in multi-cylinder combustion engines

The main source of vibrations in a multi-cylinder combustion engine is the performance of the crank and piston system, or strictly speaking, the conversion of reciprocating motion into circular motion. A kinematic analysis of a crank system may be conducted if we replace a real system with the diagram presented in Figure 1.1. The main geometric parameters characterising this diagram include [1, 2, 3, 5, 8, 9, 13, 14]:

1. length of connecting rod $l = AB$ (measured from the axis of the piston pin to the axis of the crankpin),
2. crank throw $r = BO = S / 2$,
3. piston stroke S (measured as the distance travelled by the piston between TDC and BDC),

ratio of crank throw r to the crank length $\lambda = r / l$.

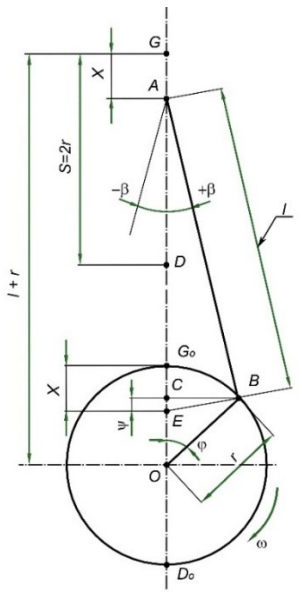

Fig. 1.1. Diagram of a simple crank system

In a real crank system the motion of the piston is not exactly harmonic. Piston velocity c in function of the angle of rotation of the shaft φ is given by [2, 3]:

$$c(\varphi) = \frac{dx}{dt} = r\omega\left(\sin\varphi + \frac{\lambda}{2}\sin 2\varphi\right) = r\omega\sin\varphi + r\omega\frac{\lambda}{2}\sin 2\varphi. \quad (1)$$

Figure 1.2 shows a graph of piston velocity *c* and its two harmonic components.

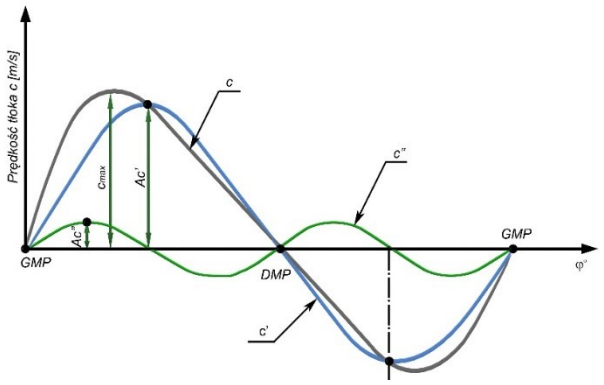

Fig. 1.2. Piston velocity $c = c' + c''$ in function of the angle of rotation of the crankshaft φ

By differentiating equation (1) with respect to time, we obtain the relation of piston acceleration *b* in function of the angle of rotation of crankshaft φ:

$$b(\varphi) = \frac{dc}{dt} = r\omega^2\cos\varphi + r\omega^2\lambda\cos 2\varphi. \quad (2)$$

Changes in constituent and resultant accelerations in function of the angle of rotation of the shaft are analysed in Figure 1.3.

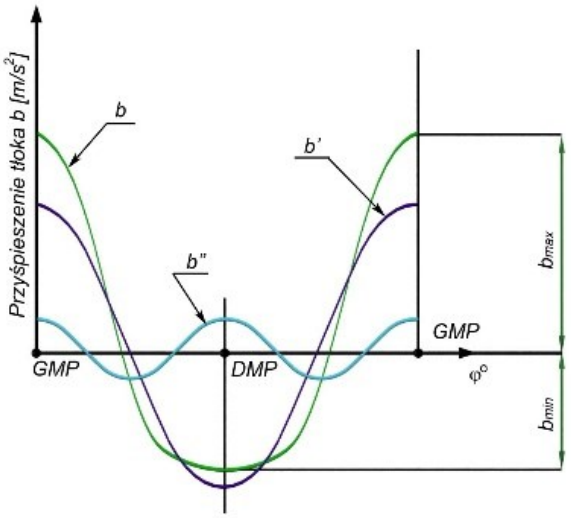

Fig. 1.3. Changes in piston acceleration $b = b' + b''$ in function of angle φ

The source of the above accelerations are forces which act upon the crank system and cause the crankshaft of the engine to vibrate. These forces include (Figure 1.4) [2, 3, 5, 13, 14]:

1. gas pressure forces generated in the mixture combustion process,
2. inertia forces originating from the masses in reciprocating and circular motion (sliding forces and centrifugal forces).

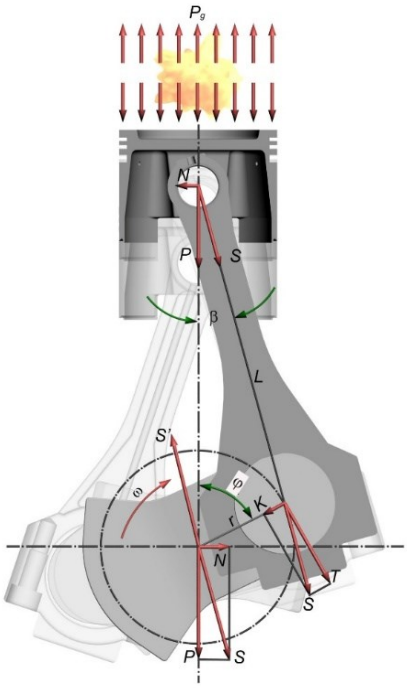

Fig. 1.4. Balance of forces in a crank and piston system

Gas pressure forces P_g and inertia forces P_b change periodically [2, 3, 1, 14]. In four-stroke engines the inertia forces change during one full turn of the crankshaft, while gas pressure forces change during two turns of the crankshaft or one full turn in two-stroke engines. The resultant force is the sum of the forces mentioned above:

$$P = P_g + P_b. \tag{3}$$

As shown in Figure 1.4, force S acts upon the crank of the crankshaft and decomposes into two components: component T tangent to the circle drawn by the crank throw and radial component K operating along the temporary location of the crank arm. The forces are characterised by the following relations:

$$T = S\,sin(\alpha + \beta) = \frac{P}{cos\,\beta} sin(\alpha + \beta), \tag{4}$$

$$K = S\,cos(\alpha + \beta) = \frac{P}{cos\,\beta} cos(\alpha + \beta). \tag{5}$$

Periodic changes in gas pressure forces P_g and inertia forces P_p generate the following types of crankshaft vibrations [2, 3, 1, 5, 14]:

1. transverse vibrations,
2. longitudinal vibrations,
3. torsional vibrations.

Vibrations are a kind of defence available to machine parts made of elastic materials, which makes them give in to the imposed load and gradually absorb the energy transferred to them.

Regardless of the dynamic system in which the engine operates, the greatest threat to the crankshaft is posed by torsional vibrations [2, 3, 1, 5, 13, 14]. The source of torsional vibrations is the periodic variability of force *T*. It is worth stressing that the scale of torsional vibrations is limited only by the torsional stiffness of the shaft and when the vibrations are not damped, their amplitude theoretically tends to infinity. Once the maximum amplitude is exceeded, the shaft breaks down.

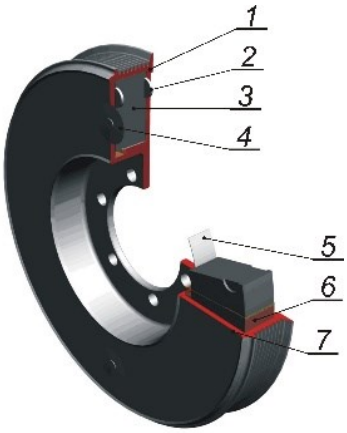

Fig. 1.5. Viscous torsional vibration damper: 1 - housing of the damper, 2 - thrust bearing, 3 - inertia ring, 4 - seal, 5 - radial bearing, 6 - silicone oil, 7 - cover

In order to minimize the threat posed by torsional vibrations, devices called torsional vibration dampers are used. Most frequently they are located at the free end of the crankshaft of the engine [2, 3]. Over the years, the following types of dampers have been used [2, 3]:

1. friction dampers,
2. viscous dampers,
3. rubber dampers,
4. spring dampers.

Viscous torsional vibration dampers are most frequently used in medium and large-size multi-cylinder combustion engines (Figure 1.5).

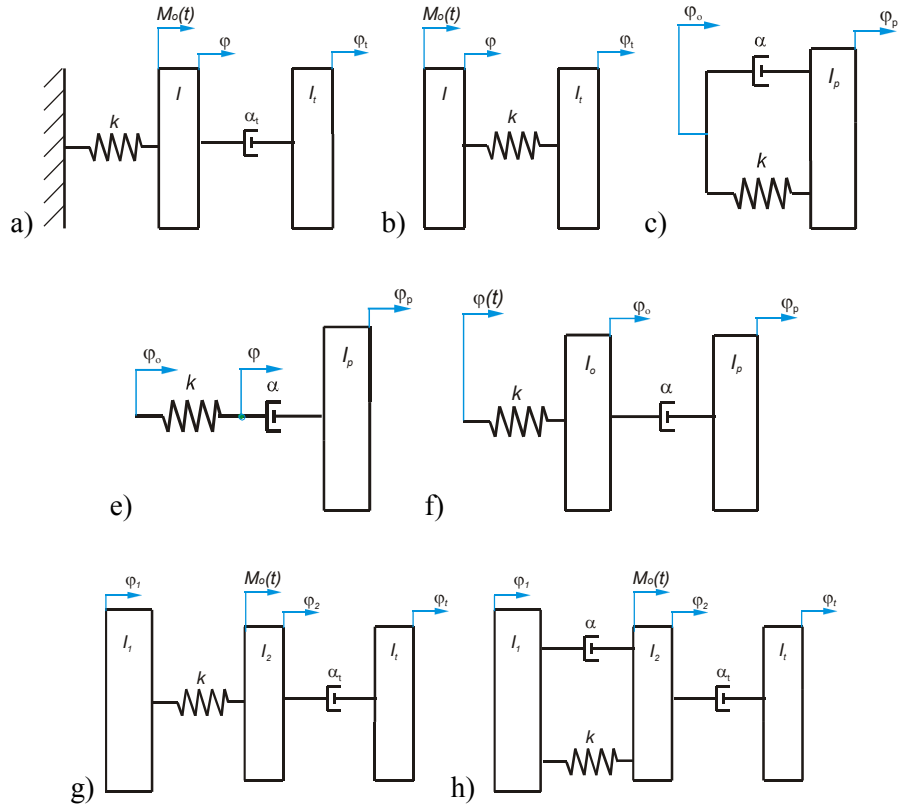

Fig. 1.6. Examples of damper modelling: a) viscous damper with torque $M(t)$ applied to the housing, b) dynamic damper with torque $M(t)$ applied to the hub, c) rubber damper with kinematic torque applied to the hub, d) viscous damper with viscoelastic fluid (Maxwell's model) with kinematic torque, e) dual mass model of a viscous damper with kinematic torque, f) model of a system comprising a viscous damper with reduced moment of inertia of the crank and piston system and torque $M(t)$ applied to the hub, g) model of a system comprising a viscous damper with reduced moment of inertia of the crank and piston system with damped inner shaft and torque $M(t)$ applied to the hub.

Viscous torsional vibration dampers are designed individually for every type of engines (power transmission systems) based on the results of a harmonic analysis of torsional vibrations in the shaft (e.g. the crankshaft or the camshaft). Before the work on designing a new damper starts, the engine producer should provide

the designer with an appropriate set of data about the engine, including data on the basic units supporting the engine [2, 3]. Based on these data, a model of the power transmission system comprising a model of the damper is built. In practice, a variety of methods are used to model torsional vibration dampers [2, 3]. Discrete systems provide an adequate approximation.

Most frequently viscous dampers are modelled as dual mass systems (Figure 1.7). The masses are interconnected by damping element α_w. Periodic torque $M(t)$ is applied to mass I_w connected with spring element k_w. The other end of the spring is immobilized, which corresponds to the node of the first form of torsional vibrations [2, 3].

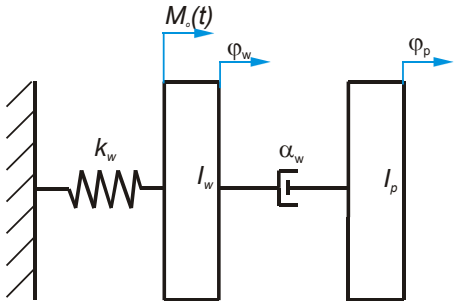

Figure 1.7. Discrete model of a viscous torsional vibration damper

Damping function α_w in a viscous torsional vibration damper depends on many variables, including in particular:

1. kinetic viscosity of the fluid,
2. dynamic viscosity of the fluid,
3. density of the fluid,
4. size of clearances,
5. mass moment of inertia of the inertia ring of the damper.

They affect the value of the damper's moment of friction, which in turn directly translates into the volume of energy dispersed by the damper [10, 15].

Analytical calculations for viscous dampers are made mainly based on models assuming linear spring element and linear damping. While the first assumption is roughly met, the second one about fluid being linear may prove to be an oversimplification, especially in the case of fluids of viscosity greater than 500,000 [cSt]. Therefore, it seems advisable to enrich the modelling of viscous torsional vibration dampers with elements of hydrodynamic modelling.

3. Elements of hydrodynamic modelling of the viscous torsional vibration damper

The discrete model presented in the previous section is quite accurate in predicting the performance of a damper in the steady state. However, it provides no information on how a damper performs in the start-up phase and when it is displaced from the steady state, e.g. by an abrupt external acceleration. The modelling of such conditions may prove particularly vital due to the fact that we are currently unable to answer the questions about mechanical damage occurring to a damper during its operation. Periodic inspections revealed dampers with seriously damaged active surfaces of the housing and the plunger, and with oil having a gel-like or even solid consistency. Since no one has yet proposed an explanation for such situations, we felt inclined to develop a model capable of at least partly explaining the reasons behind them. Therefore, in the next sections we will present certain elements of a theory of hydrodynamic modelling of the performance of a viscous torsional vibration damper.

However, before we get to that, we must define the terms and symbols that will be used later on to describe the geometry of a viscous damper. Figure 1.8 shows active surfaces of a plunger (an inertia ring in this particular case). Among others, a plunger consists of:

1. outer surface of the plunger - Figure 1.8 a),
2. lateral surface of the plunger - Figure 1.8 b),
3. inner surface of the plunger - Figure 1.8 c).

For each surface of the plunger there is a matching surface of the housing named analogically, i.e. outer surface of the housing, lateral surface of the housing and inner surface of the housing.

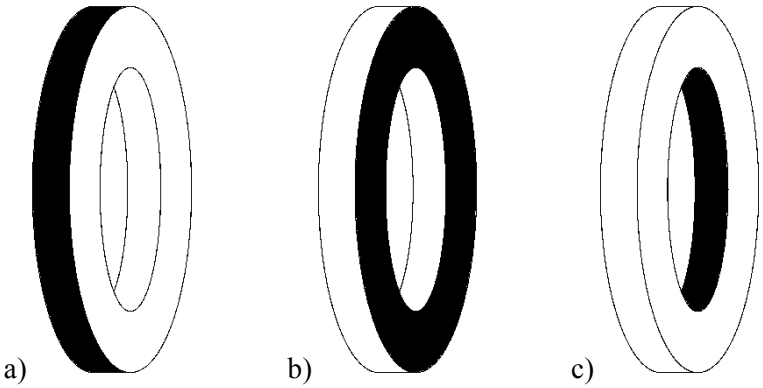

Figure 1.8. Surfaces of the plunger: a) outer surface, b) lateral surface, c) inner surface

Figure 1.9 shows the radiuses of the outer and inner surfaces of both a plunger and the housing. We make an assumption that the inner radiuses may equal 0. If that is the case, the plunger has the shape of a cylinder.

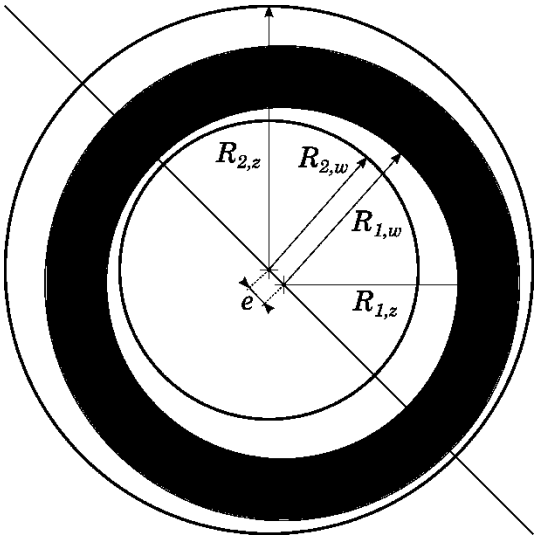

Fig. 1.9. Radiuses of the plunger and the housing: $R_{1,z}$ - outer radius of the plunger, $R_{1,w}$ - inner radius of the plunger, $R_{2,z}$ - outer radius of the housing, $R_{2,w}$ - inner radius of the housing, e - eccentricity

3.1. Basics of the rotating elements wet friction theory

At the end of the 19th century, Reynolds [11] proposed an equation for determining the pressure of a fluid film residing between two hard, moving surfaces. It turns out that if:

1. the fluid flow is laminar,
2. the force of gravity and the force of inertia are negligibly small compared to the force of viscosity,
3. the fluid is incompressible,
4. the fluid is Newtonian with constant viscosity,
5. the pressure of the fluid remains unchanged across the film's height,
6. the rate of change of velocity in directions x and z is negligibly small compared to the rate of change of velocity in direction y,
7. there is no slipping between the fluid and the surface touching it,

the fluid pressure equation takes the following form:

$$\frac{\partial}{\partial x}\left(h^3\frac{\partial p}{\partial x}\right)+\frac{\partial}{\partial z}\left(h^3\frac{\partial p}{\partial z}\right)=6\eta\left[(U_1+U_2)\frac{\partial h}{\partial x}+2V_2\right], \tag{6}$$

where η is fluid viscosity, p is pressure and the remaining values are defined in Figure 1.10.

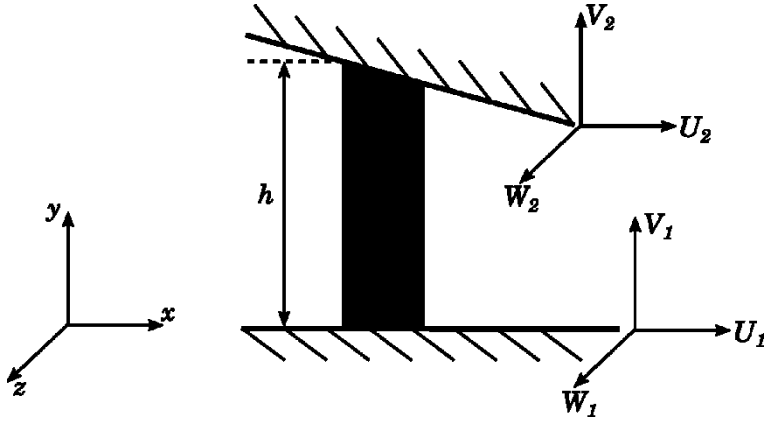

Fig. 1.10. Absolute velocities of the surfaces between which the analysed fluid resides

It must be stressed that in the form presented above the equation assumes that axis x was chosen as the direction of the relative motion of both surfaces. Consequently, we can assume that $V_1 = W_1 = W_2 = 0$. If we additionally assume that there is no flow towards axis z, the Reynolds equation is simplified to:

$$\frac{\partial}{\partial x}\left(h^3 \frac{\partial p}{\partial x}\right) = 6\eta U_1 \frac{\partial h}{\partial x}. \tag{7}$$

Using the Reynolds equation we can determine the pressure of the oil film residing between the outer and inner surfaces of the plunger and the housing. For this purpose we use a model assuming that oil does not flow in the axial direction (z) of both of these elements. In addition, we assume that ϕ from range [0, 2π] is the angular coordinate for which pressure is calculated, η is oil viscosity, R_z and R_w are outer and inner radiuses of the plunger and the housing (we assume that for the purpose of the Reynolds theory $R_z = R_{1,z} = R_{2,z}$ and $R_w = R_{1,w} = R_{2,w}$), u_z and u_w are relative velocities of the plunger and the housing respectively in the outer and inner layer, which satisfy the relation $u_z = u_w R_z/R_w$,, $c_z = R_{2,z} - R_{1,z}$ is outer radial clearance, $c_w = R_{1,w} - R_{2,w}$ is inner radial clearance, $\varepsilon_z = e/c_z$ is outer relative eccentricity, and $\varepsilon_w = e/c_w$ is inner relative eccentricity. At this point, it is worth stressing that in practice the outer radial clearance of a damper is greater than the inner radial clearance. Consequently, the plunger may touch the housing only on the inner surface on which the bearing tape is also placed. In practice, this means that the relative inner eccentricity ε_w may take values from range [0, 1]

and the relative outer eccentricity ε_z is restricted to range [0, δ], where $\delta < 1$. Using the above symbols, we can express the oil film pressure in the outer and inner slot by the following formula [4]:

$$p_\phi = \frac{6\eta u R}{c^2}\left[\int \frac{d\phi}{(1+\varepsilon\cos\phi)^2} - \frac{h_m}{c}\int \frac{d\phi}{(1+\varepsilon\cos\phi)^3}\right] + C_2, \tag{8}$$

where R is radius of curvature of the slot, u is relative velocity of the surfaces of the slot, c is radial clearance of the slot, h_m is height of the oil film where the pressure is the highest and C_2 is the integration constant.
In order to solve the following integrals:

$$\int \frac{d\phi}{(1+\varepsilon\cos\phi)^n} \tag{9}$$

we use the substitution proposed by Sommerfeld [4, 12]:

$$1 + \varepsilon\cos\phi = \frac{1-\varepsilon^2}{1-\varepsilon\cos\varphi} \tag{10}$$

where φ is a new variable with range of variation [0, 2π] – the same as for variable ϕ. In addition, the change of variables results in the following transformations $0 \to 0$, $\pi \to \pi$ and $2\pi \to 2\pi$. For a substitution expressed this way the following relations are true:

$$J_1 = \int \frac{d\phi}{(1+\varepsilon\cos\phi)} = K\varphi, \tag{11}$$

$$J_2 = \int \frac{d\phi}{(1+\varepsilon\cos\phi)^2} = K^3(\varphi - \varepsilon\sin\varphi), \tag{12}$$

$$J_3 = \int \frac{d\phi}{(1+\varepsilon\cos\phi)^3} = K^5\left(\varphi - 2\varepsilon\sin\varphi + \frac{\varepsilon^2}{2}\varphi + \frac{\varepsilon^2}{4}\sin 2\varphi\right), \tag{13}$$

where $K = 1/\sqrt{1-\varepsilon^2}$.
Using these symbols, the oil film pressure in function of angle may be expressed as follows:

$$p_\phi = \frac{6\eta u R}{c^2}\left[J_2(\varphi) - \frac{h_m}{c}J_3(\varphi)\right] + C_2, \tag{14}$$

For the completeness of the above formula it is necessary to determine integration constants h_m and C_2. We can achieve this by assuming specific pressure values. In this particular case we assume that [6]: $p_\phi(0) = p_\varphi(0) = p_0$ and $p_\phi(2\pi) = p_\varphi(2\pi) =$

p_0, while the equality of pressures $p_\phi(0) = p_\varphi(0)$ and $p_\phi(2\pi) = p_\varphi(2\pi)$ results from the fact that the applied substitution $\phi \rightarrow \varphi$ transforms $0 \rightarrow 0$ and $2\pi \rightarrow 2\pi$. Determining a specific value of p_0 is not obvious, as it depends, among others, from the absolute angular velocity of both the housing and the plunger. We will analyse this problem in greater detail further in this paper. Ultimately, for constants:

$$h_m = \frac{2(1-\varepsilon^2)}{2+\varepsilon^2} c, \tag{15}$$

$$C_2 = p_0 \tag{16}$$

and after returning to the original variable ϕ, we obtain:

$$p(\phi) = p_0 + \frac{6\eta u R}{c^2} \frac{\varepsilon(2+\varepsilon\cos\phi)\sin\phi}{(2+\varepsilon^2)(1+\varepsilon\cos\phi)^2} = p_0 + \frac{6\eta u R}{c^2}\gamma(\varepsilon,\phi), \tag{17}$$

where γ is a dimensionless distribution of the oil film pressure, whose graph for several ε values is shown in Figure 1.11.

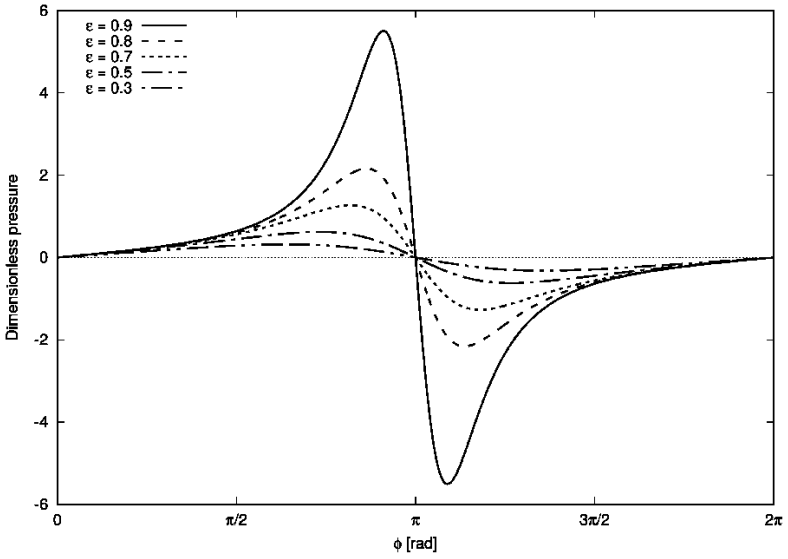

Fig. 1.11. Graph of dimensionless pressure γ for several ε values

3.2. Gümbel's condition for the inertia ring

Gümbel's condition was originally proposed for improved modelling of the oil film forces in high pressure conditions. Gümbel postulated that $p_0 = 0$ and that the negative part of pressure $p(\phi)$ equals zero. What it means is that the pressure function is exactly the same as that proposed by Sommerfeld for range $[0, \pi]$, while for range $[\pi, 2\pi]$ it equals zero. Figure 1.12 shows the parts of the oil film generating actual force under Gümbel's assumptions.

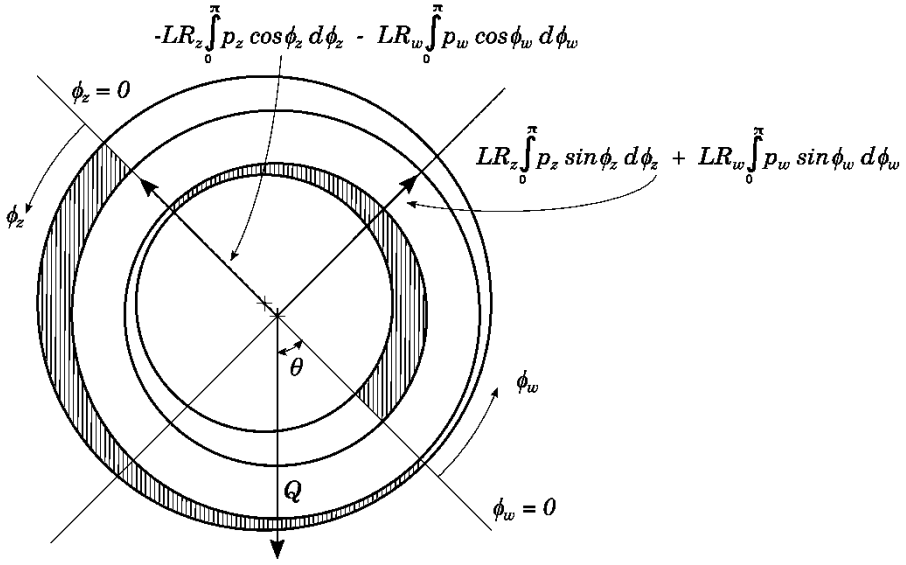

Fig. 1.12. Balance of forces for Gümbel's condition in the case of a ring-shaped plunger

An analysis of forces in the presented system leads to an equilibrium condition in which the oil film pressure entirely counterbalances the weight of the inertia ring Q.

$$Q\cos\theta = -LR_z\int_0^{\pi} p_z \cos\phi_z d\phi_z - LR_w\int_0^{\pi} p_w \cos\phi_w d\phi_w, \tag{18}$$

$$Q\sin\theta = LR_z\int_0^{\pi} p_z \sin\phi_z\, d\phi_z + LR_w\int_0^{\pi} p_w \sin\phi_w\, d\phi_w, \tag{19}$$

where L is the width of the inertia ring. In order to determine equilibrium angle θ, first we need to solve the following integrals:

$$\int_0^{\pi} p \sin\phi \, d\phi, \tag{20}$$

$$\int_0^{\pi} p \cos\phi \, d\phi. \tag{21}$$

We use integration by parts to solve both integrals:

$$\int_0^{\pi} p \sin\phi \, d\phi = [-p \cos\phi]_0^{\pi} + \int_0^{\pi} \frac{dp}{d\phi} \cos\phi \, d\phi = \int_0^{\pi} \frac{dp}{d\phi} \cos\phi \, d\phi, \tag{22}$$

$$\int_0^{\pi} p \cos\phi \, d\phi = [p \sin\phi]_0^{\pi} - \int_0^{\pi} \frac{dp}{d\phi} \sin\phi \, d\phi = -\int_0^{\pi} \frac{dp}{d\phi} \sin\phi \, d\phi, \tag{23}$$

Taking into account equation (8), we obtain:

$$\frac{dp}{d\phi} = \frac{6\eta u R}{c^2} \left[\frac{1}{(1+\varepsilon\cos\phi)^2} - \frac{h_m}{c} \frac{1}{(1+\varepsilon\cos\phi)^3} \right], \tag{24}$$

which allows us to calculate integrals (22) and (23). After making calculations for outer and inner surfaces, we obtain the following:

$$Q\cos\phi = \eta u_z L \left(\frac{R_z}{c_z}\right)^2 \frac{12\varepsilon_z^2}{(2+\varepsilon_z^2)(1-\varepsilon_z^2)} + \eta u_w L \left(\frac{R_w}{c_w}\right)^2 \frac{12\varepsilon_w^2}{(2+\varepsilon_w^2)(1-\varepsilon_w^2)}, \tag{25}$$

$$Q\sin\phi = \eta u_z L \left(\frac{R_z}{c_z}\right)^2 \frac{6\pi\varepsilon_z}{(2+\varepsilon_z^2)(1-\varepsilon_z^2)} + \eta u_w L \left(\frac{R_w}{c_w}\right)^2 \frac{6\pi\varepsilon_w}{(2+\varepsilon_w^2)(1-\varepsilon_w^2)}. \tag{26}$$

Relations (25) and (26) allow us to determine the relationship between the relative velocity of the housing and the plunger, capacity of the oil film and the shape of the slot. They will form the basis for the numerical analysis conducted below.

3.3. Numerical analysis based on real data

We conducted a numerical analysis of an actual damper characterised by the following geometric parameters: $R_{1,w}$ = 74.685 [mm], $R_{1,z}$ = 109.480 [mm], $R_{2,w}$ = 74.605 [mm], $R_{2,z}$ = 109.705 [mm] and L = 28.500 [mm]. Both the housing and the inertia ring were made of steel of density 7800 [kg/m^3]. The fluid used was silicone oil of static viscosity 300000 [cSt] = 0.3 [m^2/s] and density 1000 [kg/m^3]. Using these data and equations (25) and (26) we determine the number of turns for a given ε_w that should be made by the housing against the inertia ring so that it remains in equilibrium. At this point, it must be stressed that the results show the relative number of turns, i.e. how many more turns are made by the housing per hour. Graphs in Figures 1.13 and 1.14 show how the number of relative turns changes depending on the relative inner eccentricity ε_w. Be reminded that the relative outer eccentricity ε_z satisfies the following equation:

$$\varepsilon_z = \varepsilon_w \frac{c_w}{c_z}, \tag{27}$$

which makes ε_w the only independent variable determining the number of relative turns of both components of the damper. In the light of experiments conducted in a company manufacturing viscous dampers, the graph shown in Figure 1.14 is particularly interesting. It shows that when inner relative eccentricity ε_w equals 0.005, the housing makes one additional turn per hour. Experimental research carried out in that period produced similar results. What it means is that models assuming that the housing and the ring are concentric in the steady state are entirely justified.

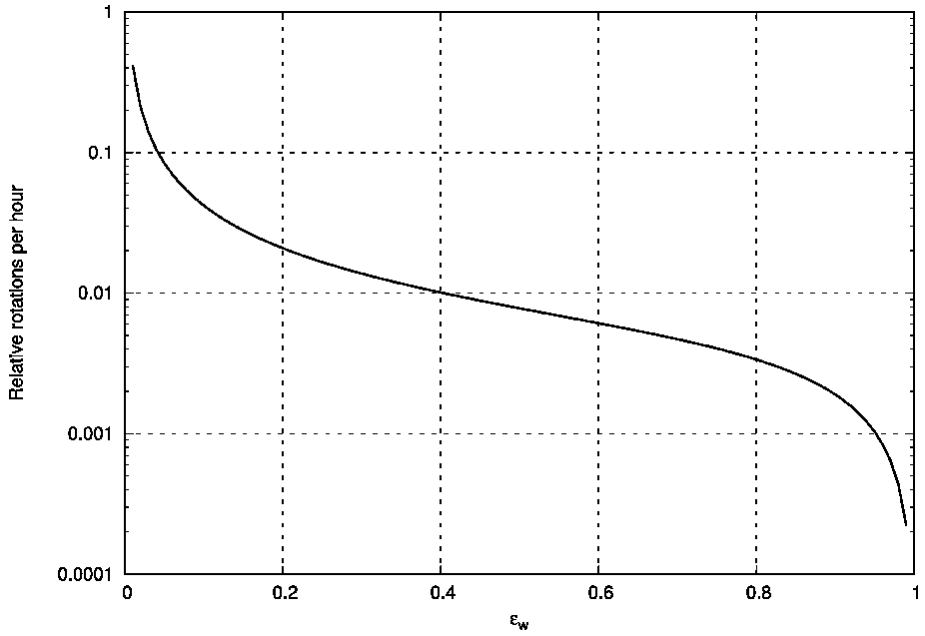

Figure 1.13. Number of turns of the housing against the inertia ring per hour, necessary for maintaining the ring in static equilibrium (range [0, 1])

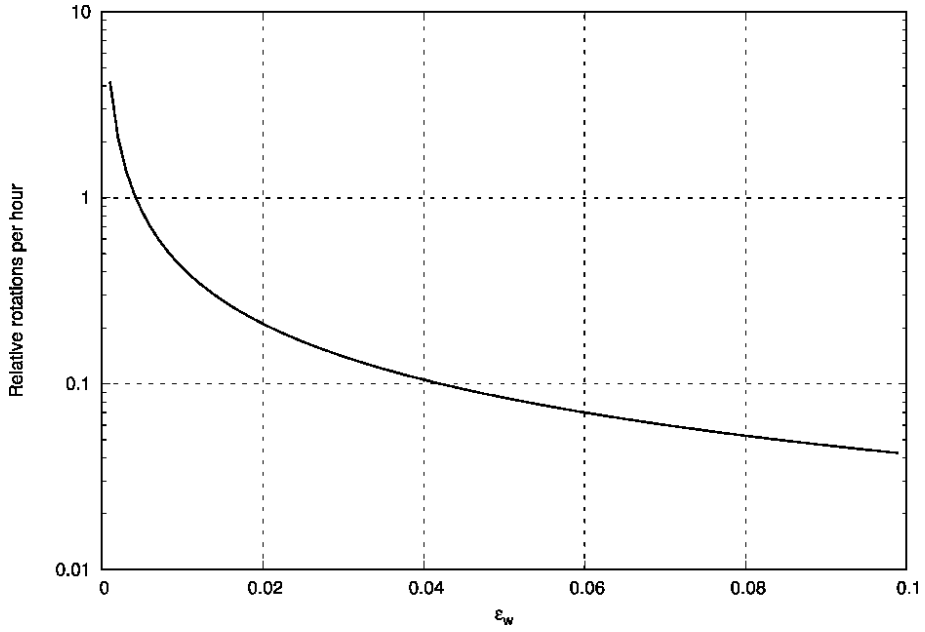

Figure 1.14. Number of turns of the housing against the inertia ring per hour, necessary for maintaining the ring in static equilibrium (range [0, 0.1])

4. Conclusions

This paper analyses the hydrodynamic effects occurring on the outer and inner surface of the inertia ring. The results of the numerical analysis conducted by the authors partially confirmed the results of experiments performed in a company manufacturing viscous dampers. Therefore, it seems legitimate to say that the presented approach is a step toward better understanding of the workings of a torsional vibration damper. However, the model outlined above does not comprehensively analyse this issue in its entirety. It must be clearly stated that the model does not cover the effects occurring on the lateral surfaces of the housing and the inertia ring, i.e. wet friction on these surfaces and increase in pressure p_0 caused by centrifugal force. The authors are continuing their research into this topic.

Research work carried out under contract No. U-18217 concluded between the DAMPOL Company implementing project no. POIR.01.01.01-00-0317/17 and the Rzeszów University of Technology. Project title: "Development of innovative technologies for the diagnosis and control of torsional vibration dampers in the crankshaft of an internal combustion engine and the selection of optimal methods for regeneration and repairs"

References

[1] Brun R. (1973). *Szybkobieżne silniki wysokoprężne*. WKiŁ.
[2] Homik W. (2012). *Szerokopasmowe tłumiki drgań skrętnych*. ITE-PIB. Radom.
[3] Homik W. (2015). *Wiskotyczne tłumiki drgań skrętnych*. ITE-PIB. Radom.
[4] Hori, Y. (2006). *Hydrodynamic Lubrication*. Springer-Verlag. Tokyo. DOI: 10.1007/4-431-27901-6
[5] Jędrzejowski J. (1986). *Mechanika układów korbowych silników samochodowych*. Wydawnictwa Komunikacji i Łacznosci, Warszawa.
[6] Langlois, W.E., Deville, M. (2014). *Slow Viscous Flow*. Springer International Publisching Switzerland. DOI: 10.1007/978-3-319-03835-3
[7] Maciotta R., Saija Merlino F. (1966). *Research on damping of torsional vibrations in the Dieselengined propelling plants*. FIAT Technical Bulletin 2.
[8] Niewiarowski K. (1986). *Tłokowe silniki spalinowe*. WKiŁ. Warszawa.
[9] Parszewski Z. (1976). *Teoria maszyn i mechanizmów*. WNT. Warszawa.
[10] Płowiec R. (1990). *Lepkość i sprężystość cieczy określana za pomocą ultradźwiękowych fal ścinania*. PWN. Warszawa - Poznań.
[11] Reynolds, O. (1886). On the Theory of Lubrication and its Application to Mr. B. Tower's Experiments. *Philosophical Transaction of Royal Society of London*. Vol. 177(1). pp. 157-234.
[12] Sommerfeld, A. (1904). Zur hydrodynamischen Theorie der Schmiermittelreibung. *Zeit. angew. Math. u. Physik*. Vol. 50. pp. 97-155.
[13] Wajand J.A. (1988). *Silniki o zapłonie samoczynnym*. WNT. Warszawa.
[14] Wajand J.A, Wajand J.T. (1993). *Tłokowe silniki spalinowe średnio i szybkoobrotowe*. WNT. Warszawa.
[15] Willkinson W. (1963). *L Ciecze nienewtonowskie*. WNT. Warszawa.

Chapter 2.

Piotr TARNAWSKI[1*]
Wiesław OSTAPSKI[1]

TURBINE ENGINE CONCEPT REALIZING HUMPHREY CYCLE

Abstract

A characteristic feature, and at the same time the main assumption of presented engine concept, is the isochoric combustion process, which takes place in stationary combustion chambers. The engine works according to Humphrey's thermodynamic cycle, which has higher theoretical energy efficiency than Brytona-Joule cycle, according which work classical turbine engines. The operation of investigated engine concept requires consecutive stages of: preparation of high-pressure gases and supplying the turbine with these gases. The engine is powered by pulses, completely different than classical turbine engines, which are continuously powered. Realization of pulse powering requires the use of the valve timing system. It is crucial element of presented engine concept, and has decisive impact on its effective operation. The presented analysis has conceptual-computational character. The 3-dimensional numerical analysis of CFD (Computational Fluid Dynamics) was research tool. The gas flow in the mobile valve system, combustion process, gas expansion and moment generation in the turbine was simulated and analysed. The several created intermediate valve timing concepts have led to the development of innovatory rotating valve timing system, which provided big internal energy efficiency of engine.

Keywords:
turbine engine, helicopter drive, isochoric combustion, Humphrey cycle, pressure gain combustion, valve timing system, energy efficiency, specific fuel consumption, computational fluid dynamics

1. Introduction to internal combustion engine development

1.1. Refining of engine designs known for years

One of the most important parameters that characterizes contemporary engines is specific fuel consumption. Since the first engine concept, engineers

[1] Institute of Machine Design Fundamentals, Warsaw University of Technology, Narbutta 84, 02-524 Warsaw, Poland
[*]e-mail: piotr.tarnawski@pw.edu.pl

throughout the world have made a continuous effort to improve its energy efficiency and thus reduce specific fuel consumption. The challenge is motivated by the desire for thermodynamic perfection of the machine, as well as by its economic and environmentally friendly aspect. The lower the fuel consumption, the lower operating costs, and the less harmful exhaust gases entering the atmosphere [1].

A specific area of application of internal combustion engines is helicopter drives. The lifting power of the flying object is produced indirectly due to the rotational motion of the rotor driven by the engine. Two types of engines are used: piston engines or turbofan engines. It is worth noting that due to better performance (large thrust, bigger flight speed, smaller overall dimensions, lower mass, higher driving efficiency) [2], turbine engines are the most common type of engine used for helicopter drives.

Recent years of engines development field has focused on increasing the inlet air pressure, improving the thermal strength of construction materials, and improving the aerodynamic efficiency of components (compressors, turbines, and others) [3], [4], [5].

One of the best in its class is the turboshaft engine of General Electric T700 (1775 kW) [6], whose energy efficiency is 0.319 and a specific fuel consumption is 263.4 g / kWh. The second example is the Rolls-Royce Turbomeca RTM322 engine (1799 kW), which has an energy efficiency of 0.321 and a specific fuel consumption of 261.8 g / kWh [7] (Table 1.1).

Table 1.1. Performance parameters of contemporary turboshaft engines

Contemporary turboshaft engines	Energy efficiency	Specific fuel consuption [g/kWh]
Rolls-Roys, (190 kW)	0.188	468,0
Pratt and Whitney Canada, PW 100, (2050 kW)	0.291	290,0
General Electric T700, (1967 kW)	0.319	263,4
Rolls-Royce Turbomeca RTM322 (1799 kW),	0.321	261,8

1.2 Different direction of development of internal combustion engines

A different direction of development of internal combustion engines is concentrated around the issue of the gas pressure increase during the combustion process [8], [9] (ang. Pressure Gain Combustion). The pressure

increase can be achieved by burning in a constant volume chamber or by detonation combustion [9], [10]. This idea assumes that in a turbine engine system conventional combustion chambers are replaced by combustion chambers generating the pressure increase (Fig. 2.1).

The efforts related to the development of this area of knowledge is interesting because the thermodynamic cycle of the engine changes. As a result completely new ideas for the engine construction appears [11], [12], [13], [14], [15].

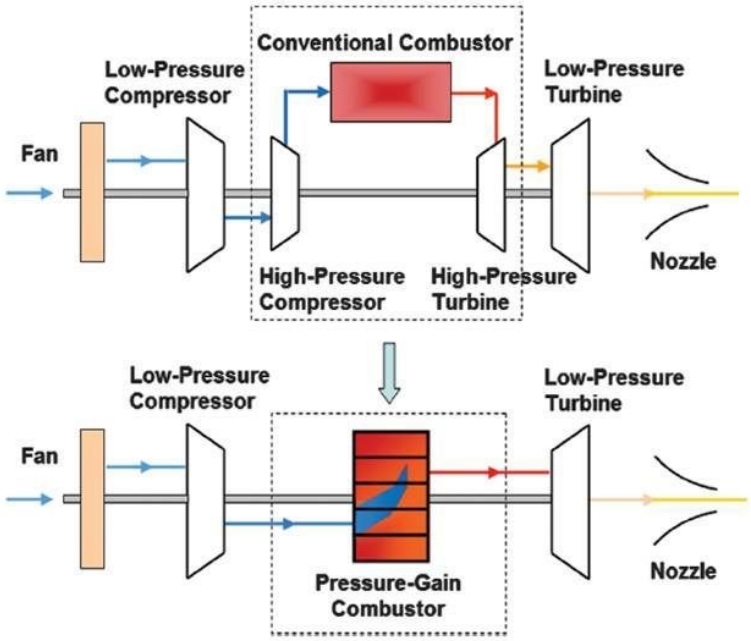

Fig. 2.1. Turbine engine scheme using combustion chambers generating pressure increase [1]

The pressure increase during isochoric combustion is a fundamental and well-known thermodynamic process [16]. The first attempts to use it for a turbine engine application was carried out in 1900 by Holzwarth [17], [18], [19]. Other attempts [20], [21] sought to improve engine efficiency, but no commercial application of an engine with constant volume chambers is known. The basic challenge is complicated to implement the effective process of conversion of a high-pressure gas impulse into mechanical energy. The most common causes are the idle period and the changing thermal parameters of the gas. This leads to an interruption of the expansion process, inefficient gas flow, partial turbine load, and complex mechanical valve timing design [22], [23].

1.3 The energy efficiency advantage of Humphrey cycle over the Britan-Joule cycle

The classic turbine engine works according to the Brayton-Joule cycle. It consists of two isobaric processes (combustion and exhaust) and two isentropic processes (compression and expansion) (Fig. 2.2). The energy efficiency of the Briton-Joule cycle was equal 0.53 [Eq (1)]. The calculation where done assuming ambient parameters equal to T = 283 K and p = 0.1 MPa (point 1) and isentropic compression to 1.4 MPa:

$$\eta_{EB-J} = \frac{l_{B-J}}{q_d} = \frac{q_{in} - q_{out}}{q_{in}} = \frac{T_2 - T_1}{T_2} = 1 - \frac{1}{\pi^{\frac{k-1}{k}}} \quad \text{where:} \quad \pi = \frac{p_2}{p_1} \tag{1}$$

where: η_{EB-J} [-] – energy efficiency of Brytona-Joule cycle, l_{B-J} [J/kg] – work done in Bryton-Joule cycle, q_{in} [J/kg] – heat supplied, q_{out} [J/kg] – heat exhausted, T_2 [K] – temperature after compression, T_1 [K] – ambient temperature, π – compression ratio, p_1 (Pa) - ambient pressure; p_2 (Pa) - pressure after compression (Pa).

The Humphrey cycle can be treated as a modification of the Brayton-Joule cycle, because only the combustion process is different. Namely combustion takes place at a constant volume, while the rest process remain unchanged. The energy efficiency of the Humphrey cycle reached 0.64 [Eq. (2)]:

$$\eta_{EH} = \frac{l_H}{q_d} = \frac{q_d - q_w}{q_d} = 1 - \frac{c_p(T_4 - T_1)}{c_v(T_3 - T_2)} = 1 - k\frac{1}{\pi^{\frac{k-1}{k}}}\frac{\lambda^{\frac{1}{k}} - 1}{\lambda - 1} \tag{2}$$

where: η_{EH} - energy efficiency of Humphrey cycle, l_H [J/kg] - work done in Humphrey cycle, c_v [J/kgK] – constant volume heat capacity, c_p [J/kgK] – constant pressure heat capacity, T_3 (K) maximal cycle temperature, p_3 = maximal cycle pressure (Pa).

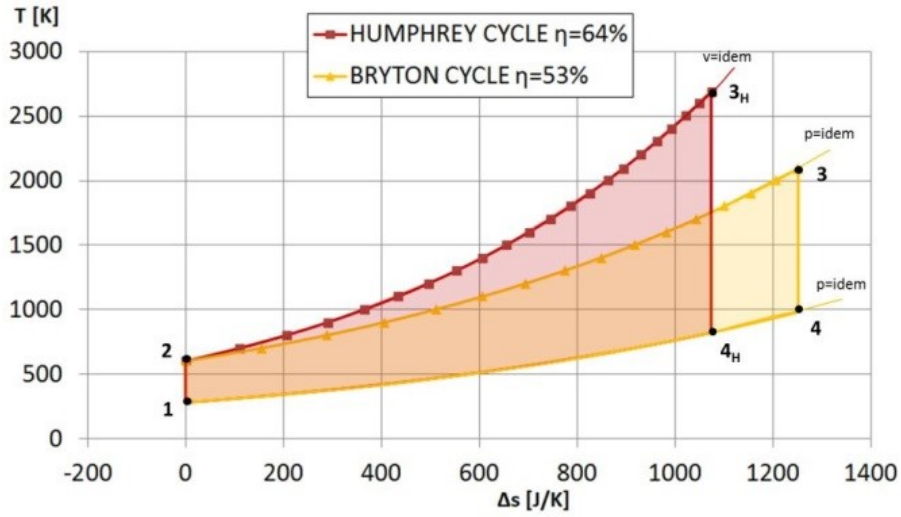

Fig. 2.2. Comparison of Bryton-Joule cycle and Humphrey cycle

The Humphrey cycle reached 11% higher energy efficiency. Higher efficiency is a result of achieving higher peak pressure and temperature in the combustion process. The result gives reasonable grounds for attempts creating an engine working according to the Humphrey cycle [24].

2. Turbine engine concept realizing Humphrey cycle

2.1. Principle of operation of pulse powered turbine engine

The classical turbine engine operating according to the Bryton-Joule cycle is continuously powered. In contrast, the work of the engine operating according to the Humphrey cycle must have a pulsating character. The generating power is interrupted by the following stages of preparation of high-pressure gas and supplying the turbine with these gases. The engine should work according to a repeating cycle which consists of: filling, isochoric combustion and gas exhaust to turbine. Realization of pulse powering requires the use of the valve timing system. It is crucial element of presented engine concept, and has decisive impact on its effective operation [23].

2.2. Virtual prototyping using numerical fluid mechanics

The 3-dimensional numerical analysis of CFD (Computational Fluid Dynamics) was research of engine concept. It gives huge possibilities of creation and refinements of thermal device, while saving the time required and economic demand. The computer model of the device can be easily and quickly corrected, approaching the best of its performance.

The gas flow in the mobile valve system, combustion process, gas expansion and torque generation in the turbine was simulated. A engine work with

application of valve timing system using various types of valves and with different supplying variants (supplying on the entire circumference of the turbine, application of 2-pressure nozzles) was investigated. The analyzed intermediate valve timing concepts have led to the development of innovatory rotating valve timing system, which is presented in next subsection. Intermediate valve timing concepts can be found in work [25] and [26].

With the help of the commercial ANSYS Fluent software package, transient Navier-Stokes [Eq. (4)-(7)] for three dimensions were solved, together with the energy [Eq. (8)] and the Clapeyron [Eq. (9)] for compressible and semi-perfect model of fluid in turbulent regime of flow as well as the transport of individual gas components [Eq. (10) and (11)] with included combustion reaction [Eq.(12)].

$$\frac{\mathrm{D}\rho}{\partial t} + \rho\left(\frac{\partial w_x}{\partial x} + \frac{\partial w_y}{\partial y} + \frac{\partial w_z}{\partial z}\right) = 0 \tag{4}$$

$$\rho\frac{\mathrm{D}\overline{w}_x}{\mathrm{D}t} = \left(\frac{\partial \bar{\tau}_{xx}}{\partial x} + \frac{\partial \bar{\tau}_{yx}}{\partial y} + \frac{\partial \bar{\tau}_{zx}}{\partial z}\right)_{\mathrm{lam}} + \left(\frac{\partial \bar{\tau}_{xx}}{\partial x} + \frac{\partial \bar{\tau}_{yx}}{\partial y} + \frac{\partial \bar{\tau}_{zx}}{\partial z}\right)_{\mathrm{turb}} \tag{5}$$

$$\rho\frac{\mathrm{D}\overline{w}_y}{\mathrm{D}t} = \left(\frac{\partial \bar{\tau}_{xy}}{\partial x} + \frac{\partial \bar{\tau}_{yy}}{\partial y} + \frac{\partial \bar{\tau}_{zy}}{\partial z}\right)_{\mathrm{lam}} + \left(\frac{\partial \bar{\tau}_{xy}}{\partial x} + \frac{\partial \bar{\tau}_{yy}}{\partial y} + \frac{\partial \bar{\tau}_{zy}}{\partial z}\right)_{\mathrm{turb}} \tag{6}$$

$$\rho\frac{\mathrm{D}\overline{w}_z}{\mathrm{D}t} = \left(\frac{\partial \bar{\tau}_{xz}}{\partial x} + \frac{\partial \bar{\tau}_{yz}}{\partial y} + \frac{\partial \bar{\tau}_{zz}}{\partial z}\right)_{\mathrm{lam}} + \left(\frac{\partial \bar{\tau}_{xz}}{\partial x} + \frac{\partial \bar{\tau}_{yz}}{\partial y} + \frac{\partial \bar{\tau}_{zz}}{\partial z}\right)_{\mathrm{turb}} \tag{7}$$

$$\rho\left[\frac{\partial i}{\partial t} + \overline{w}\,\nabla i\right] = \nabla\cdot(k_{eff}\nabla T) + \frac{Dp}{Dt} + \mu\Phi + S_h \tag{8}$$

$$p = \rho\mathrm{R}T \tag{9}$$

$$\rho\frac{\mathrm{D}Y_i}{\mathrm{D}t} = -\nabla\cdot J_i + R_i \tag{10}$$

$$S_h = -\Sigma_j \frac{h_i^{\,o}}{M_i} R_i \tag{11}$$

$$R_i = \nu' M_i A \rho \frac{\varepsilon}{k} \left(\frac{Y_R}{\nu'_R M_R}\right) \quad \text{or} \quad R_i = \nu''_i M_i AB \rho \frac{\varepsilon}{k} \left(\frac{\sum_P Y_P}{\sum_j^N \nu''_j M_j}\right) \qquad (12)$$

where: t [s] - time, ρ [kg/m3] – density, p [Pa] – pressure, $\overline{w_i}$ [m/s] - averaged velocity component for i = x; y; z; $(\overline{\tau_{i,j}})_{\text{lam}}$ [Pa] - average tensor of shear stress of laminar origin for directions i; j = x; y; z; $(\overline{\tau_{i,j}})_{\text{turb}}$ [Pa] - average tensor of shear stress of turbulent origin; i [J] – enthalpy, T [K] – temperature, k_{eff} [W/mK] – effective heat conductivity, Φ [J] – Energy dissipation function associated with friction, S_h [W/m^3] heat source from chemical reaction; R [J/kgK] – gas constant, Y_i [-] - gram fraction of the i_{th} species of the gas mixture, J_i [kg/s] - diffusion stream of the i_{th} component, R_i [kg/s] – the generation of the i_{th} species as a result of a chemical reaction.

2.3. Pulse powered turbine engine concept – CFD simulation results

The presented engine concept is the result of a gradual correction and elimination of its defects. The final version consists of 6 chambers with a volume of 1500 cm3 each located on the circumference of the turbine, 3-nozzle rotating valve timing system positioned symmetrically, turbine and stationary component of turbocharger gas exhaust (Fig. 2.3). After filling the chamber with compressed air isochoric combustion takes place. Then the rotating nozzles successively empty the chambers and supply the turbine with high velocity gas. The valve timing system was construct to alleviate pulse powering character. Emptying of a single chamber take place in three stages: through a high pressure nozzle, then through a medium pressure nozzle and finally through a low pressure nozzle. Different ratios of nozzle sections ensure effective gas expansion for changing pressure range. The ratio of the outlet cross-section area to the minimal cross-section area is as follows:

- for high pressure nozzle 4,7,
- for medium pressure nozzle 2,6,
- for low pressure nozzle 1,4.

Between the symmetrically group of nozzles there is a gap. This is the period when the chambers are closed. During this time, high-pressure gas is prepared (filling, direct fuel injection and combustion).

Rotating valve timing system is single element and self-propelled object, whose rotation is caused by the jet force generated in the nozzles. Rotational speed 1537 rpm system ensured realization of given engine cycle. The turbine rotated in the opposite direction at 32000 rpm. The numerical mesh used in the simulation is presented in Fig. 2.4. It consisted of 450000 of hexahedral elements. The turbulence was modeled with realizable k-e model. The boundary layer was resolved using a standard wall functions.

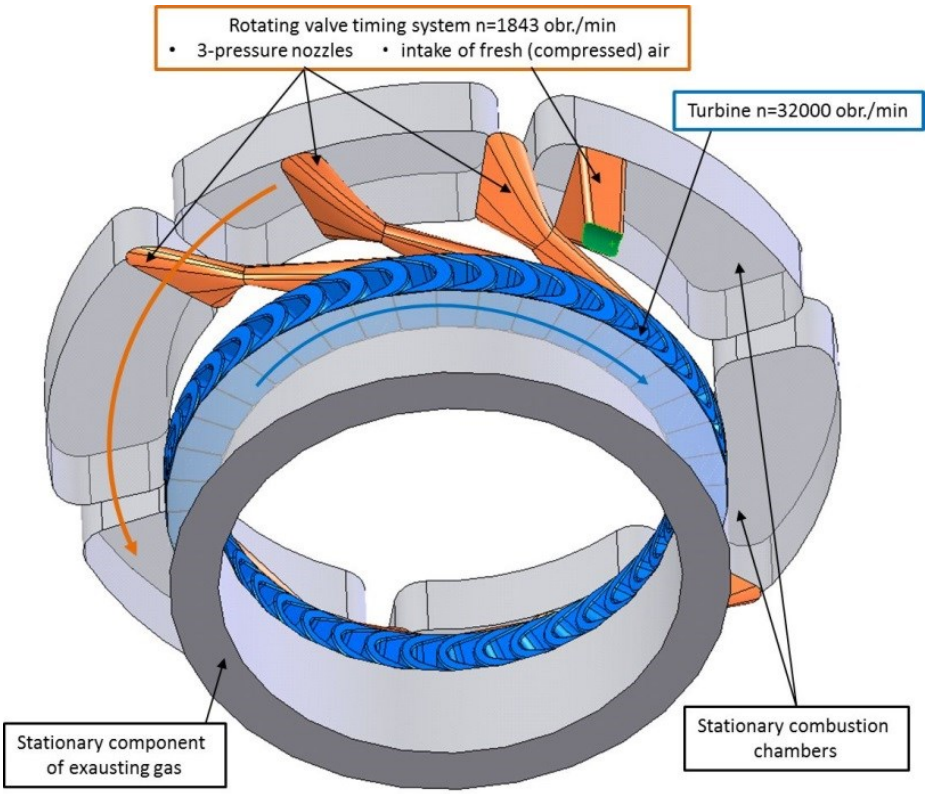

Fig. 2.3. Simulation model of engine implementing rotating valve timing system with 3-pressure nozzles

The temperature in the chamber between the individual combustion cycles is shown in Fig. 2.5. As a result of combustion, the temperature of the gases rose from 850 K to a maximum value of 2390 K. Then the exhaust gas flowed into the turbine successively through the high pressure nozzle, through the medium pressure nozzle, and finally through the low pressure nozzle. As a result of the exhaust flow, the temperature of the gas in the chamber decreased. At the end of cycle an inflow of cold compressed air was realized. This was followed by another combustion cycle. The average temperature in the chamber was about 1800 K.

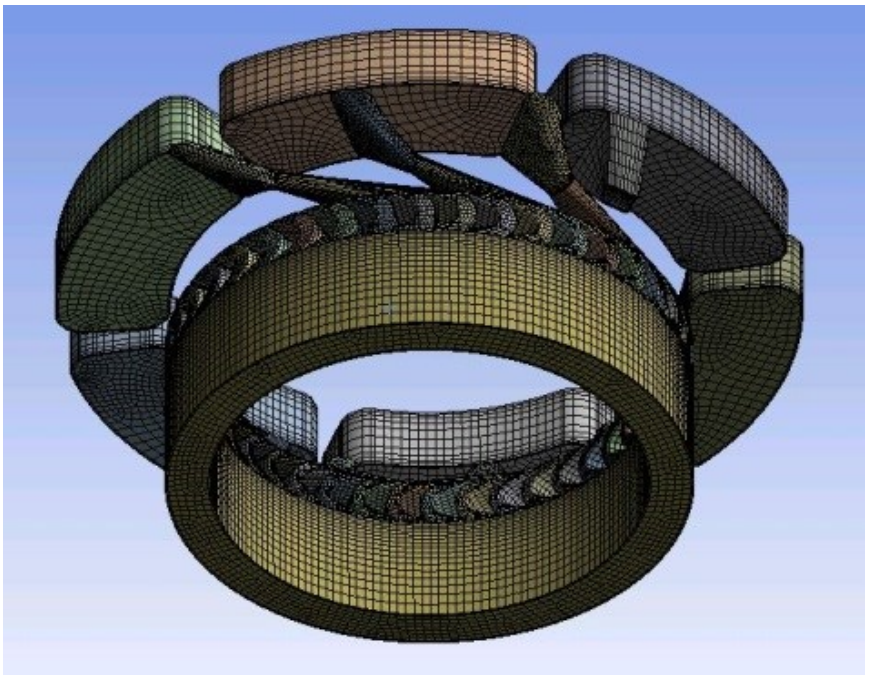

Fig. 2.4. Numerical mesh of engine simulation model

The simulation included cooling of the chamber walls. The wall temperature was assumed to 1300°C.Thermal resistance of walls can be achieved using thermal barrier coating (27). The heat transfer was carried out by convective and irradiative mode. Direct injection of fuel (diesel oil) was assumed, which after ignition was self-igniting (26).

The pressure change in the chamber between the individual combustion cycles is shown in Fig. 2.6. As a result of isochoric combustion, the pressure increased from 1.95 MPa to 5.4 MPa. The gas exhaust through the high pressure nozzle lowered the pressure in the chamber to 4.2 MPa, then gas exhaust through the medium pressure nozzle lowered the pressure in the chamber to 2.3 MPa, at the end the gas exhaust through the low pressure nozzle lowered the pressure in the chamber to 1.5 MPa. Filling the chamber with compressed air proceeded at only slight increase in pressure (almost isobaric). The air compression was assumed to be realized in two stages with the use of external devices: in turbochargers up to 0.45 MPa (using the kinetic energy of exhaust gases behind the turbine) and in a centrifugal mechanical compressor up to 1.6 MPa (using mechanical energy from turbine shaft).

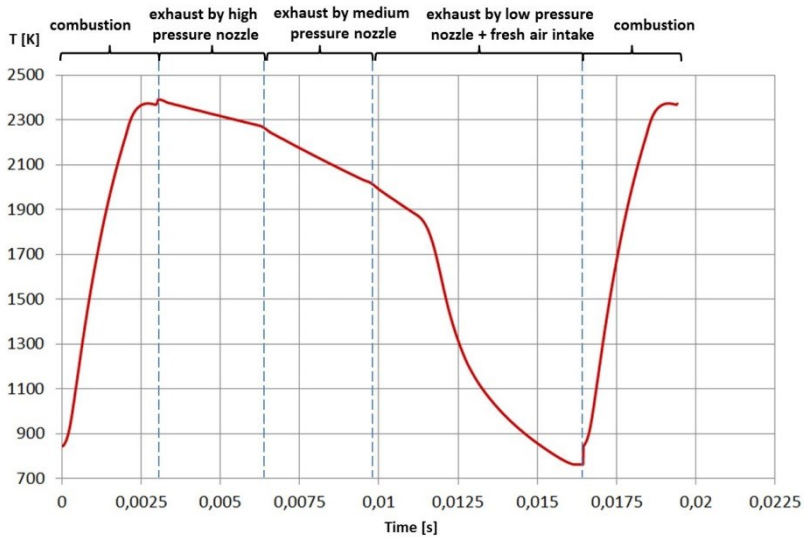

Fig. 2.5. Temperature change in combustion chamber for single engine cycle

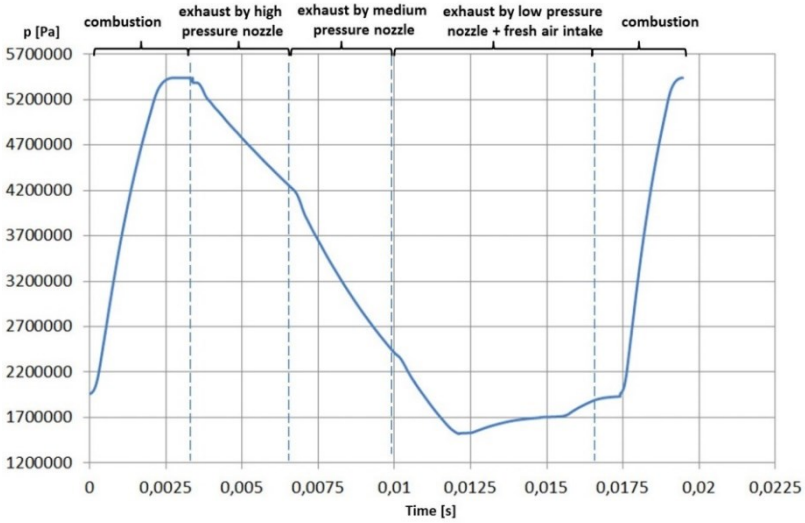

Fig. 2.6. Pressure change in combustion chamber for single engine cycle

The fresh air intake was located just after the low pressure nozzle Fig. 2.7. The filling of the chamber with fresh was is carried out simultaneously with the gas exhaust through the low pressure nozzle. The process has been aimed

to prevent a fresh air leak to the low pressure nozzle and to minimize the mixing of fresh air with the combustion gas**.**

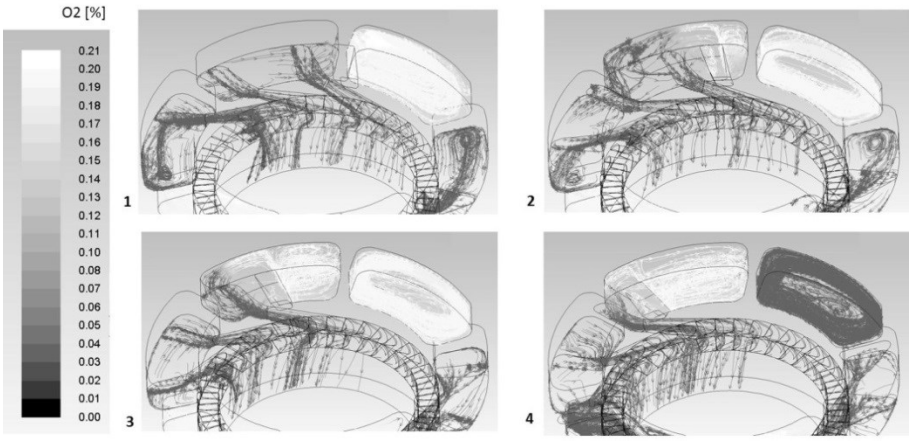

Fig. 2.7. Percentage oxygen content of flowing gas during filling

During the expansion process a gas pressure was decreasing in nozzles, reaching the lowest 0.1 MPa value at the turbine outlet, as shown in Fig. 2.8.

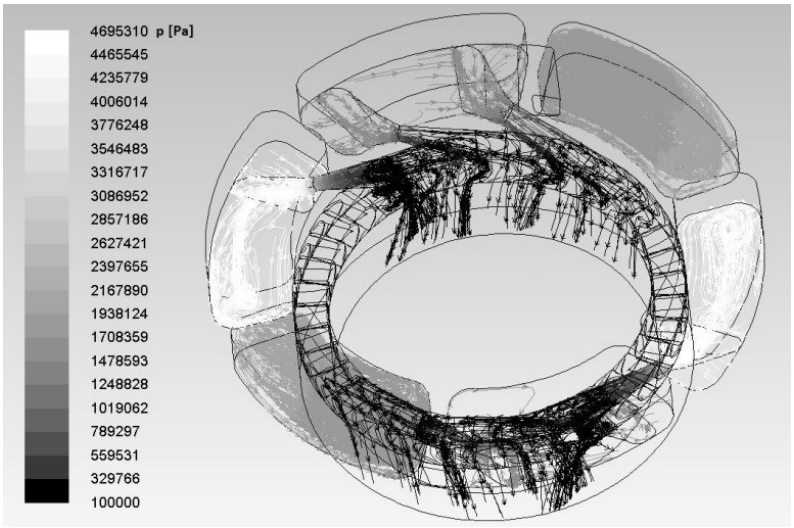

Fig. 2.8. Pressure distribution of flowing gas

The velocity of exhaust gas in the different nozzles varied. The largest values were in the high-pressure nozzle (2.5 Mach), and the smallest in the low-pressure nozzle(1.5 Mach). The distribution of the Mach number is shown in Fig. 2.9.

As the gas velocity in nozzles was increasing, the gas temperature was decreasing (Fig. 2.10). The temperature of the exhaust gas in the space between the blades was different. The highest value of 1500 K occurred after leaving the high pressure nozzle, and the lowest 1100 K after leaving the low pressure nozzle (Fig. 2.11). The different temperatures gases flowing through the blades followed each other. After the higher temperature flow followed lower temperature flow. It had a special advantage, namely it can be treated as the form of self-cooling turbine blades.

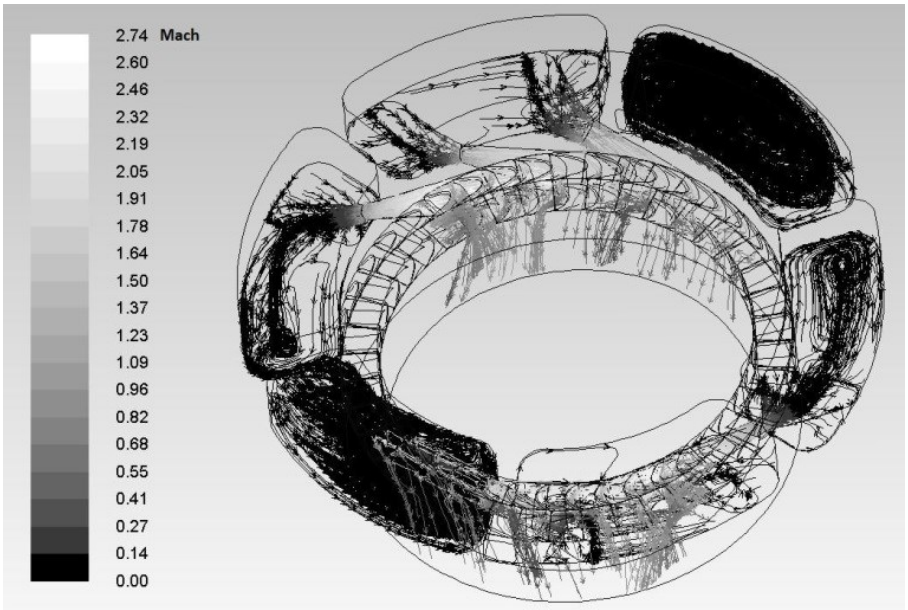

Fig. 2.9. Mach number distribution of flowing gas

The gas velocity at the outlet of the three nozzles was different. The highest velocity occurred in the high pressure nozzle and the lowest velocity was in the low pressure nozzle. In addition, the velocity of the exhaust gas in the nozzles varied over time, e.g. in the high-pressure nozzle the speed varied from 1700 m / s to 1525 m / s (Fig. 2.12).

The optimal angle α between the nozzles and the turbine axis should ensure tangential attack of the flowing gas on the turbine blades. The tangential attack of the flowing gas prevents detaching of flow from turbine blades, providing

greater internal efficiency of the turbine. The attack angle of the nozzles was determined on the basis of the velocity triangle (Fig. 2.13).

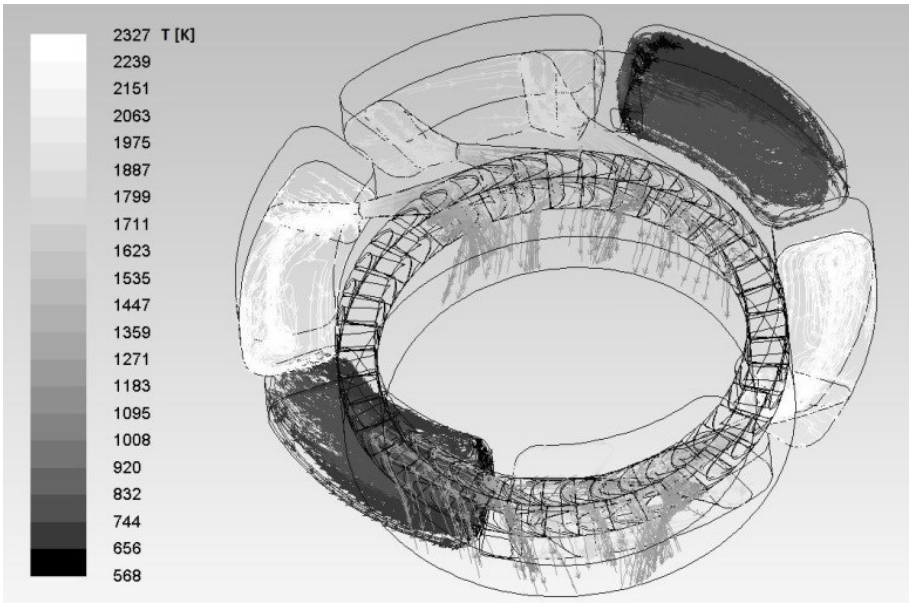

Fig. 2.10. Temperature distribution of flowing gas

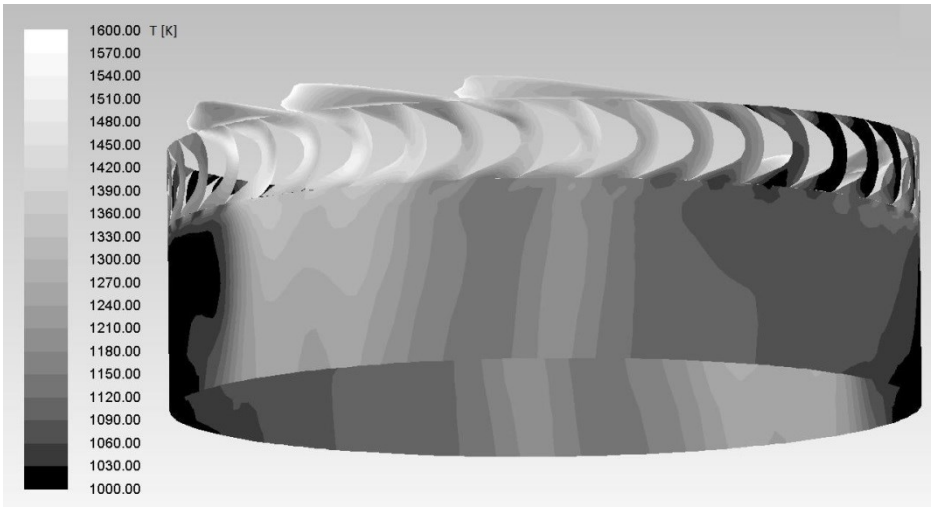

Fig. 2.11. Temperature distribution in vicinity of turbine blades

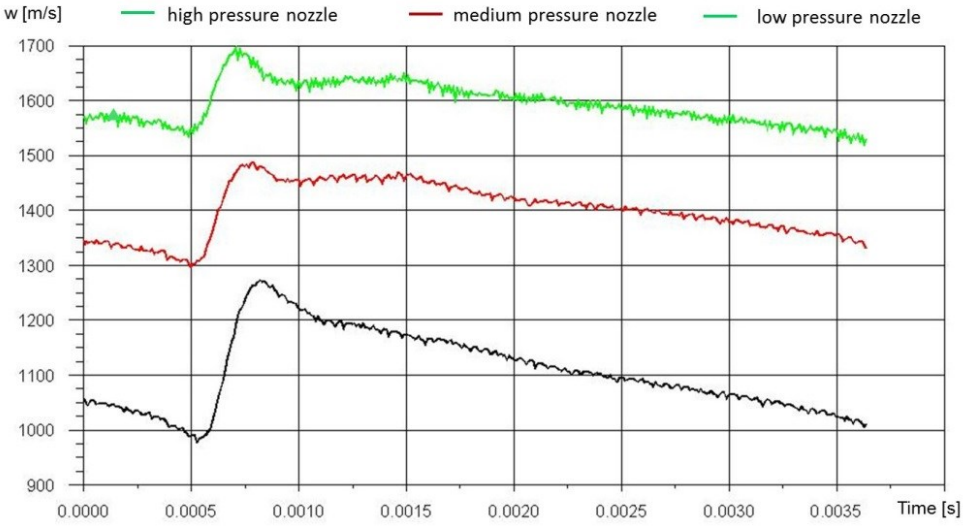

Fig. 2.12. Velocity change of flowing gas for three different nozzles

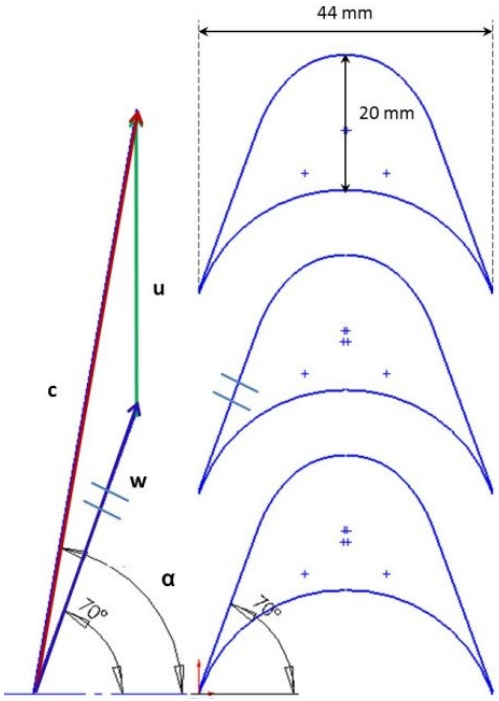

Fig. 2.13. Velocity triangle for gas flowing into turbine together with turbine blade profile

At the known absolute velocity of the flowing gas and the peripheral speed of the turbine, an optimal angle α can be determined, ensuring tangential attack of the flowing gas into the turbine. For an average gas velocity of 1660 m/s in the high pressure nozzle, the optimal angle was equal 78 degrees. For an average gas velocity of 1350 m/s in the medium pressure nozzle, the optimal angle was 80 degrees. For an average velocity of 1140 m/s in the low-pressure nozzle, the optimum angle was 82 degrees. The dependence of the angle α on the optimal gas velocity is shown in Fig. 2.14.

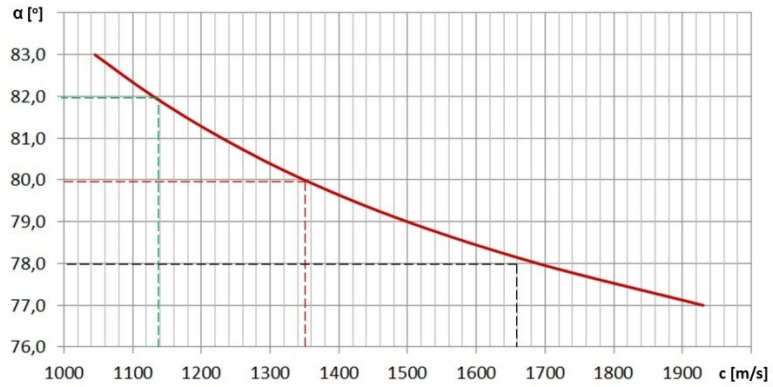

Fig. 2.14. The dependence of the optimum angle of attack α from gas velocity c

The turbine moment generation was caused by pressure difference between two side of blades. The pressure distribution in vicinity of blades is presented in Fig. 2.15.

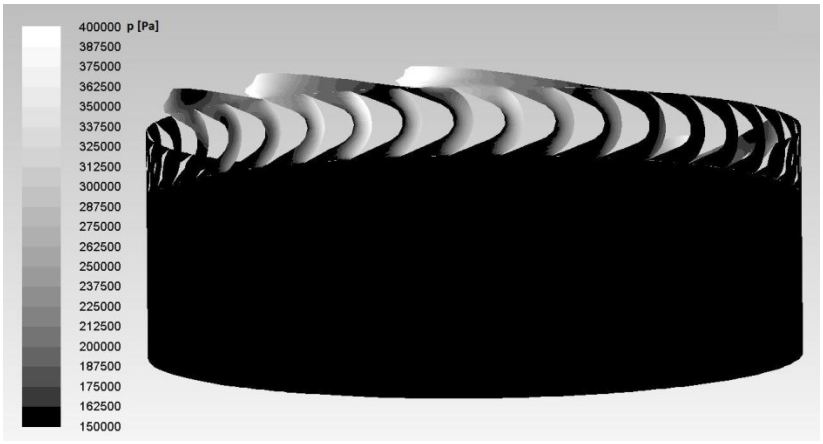

Fig. 2.15. Pressure distribution in vicinity of blades

The moment generated in the turbine ranged from a maximum of -1200 Nm to a minimum of -710 Nm (Fig. 2.16). The average torque value was equal -941 Nm. The negative moment value results from the assumed direction of turbine rotation.

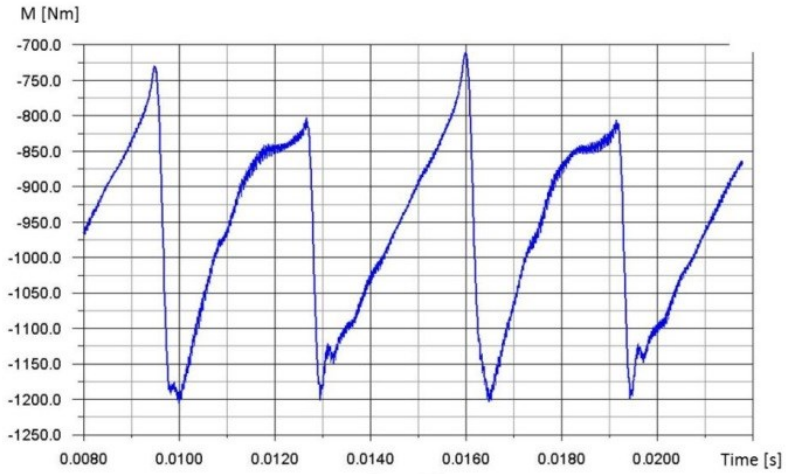

Fig. 2.16. Moment generated in turbine for two engine pulses

The moment generating the work occurred also in the rotating valve timing system. Its value ranged from a maximum of 1000 Nm to a minimum of 675 Nm (Fig. 2.17). The averaged moment was equal 837 Nm.

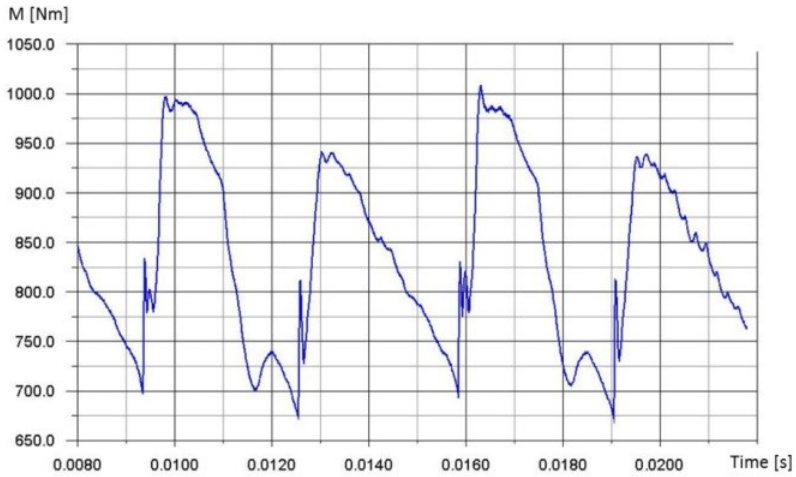

Fig. 2.17. Moment generated in rotating valve timing system for two pulses

Calculation of the energy efficiency of the engine was carried out for single power pulse (0.0065 s). During this period, 2 chambers were emptied. Chemical energy was calculated according to [Eq. (13)]:

$$E_{chem} = l \cdot m_{fuel} \cdot W_d \tag{13}$$

where: E_{chem} [J] – chemical energy of fuel, l – number of chambers, m_{fuel} [kg] – mass of fuel W_d [J/kg] – caloric value of fuel.
The internal work done by the turbine was calculated according to [Eq. (14)]:

$$L_{iT} = \frac{M_T \cdot n \cdot t_{cycle}}{9549} \tag{14}$$

where: L_{iT} [kJ] – turbine internal work, M_T [Nm] – moment generated in turbine, n [obr./min] – rotational speed of turbine, t_{cycle} [s] – length of the cycle.
Mechanical efficiency 0.95 was assumed the same for turbine and rotating valve timing system. Effective work produced by turbine calculated according to [Eq. (15)] :

$$L_{eT} = L_{iT}\eta_{mT} \tag{15}$$

where: L_{eT} – [kJ] – effective work of turbine, η_{mT} [-] – mechanical efficiency of turbine.

Effective work of engine was difference of energy produced (effective work of turbine i kinetic energy of gas at turbine outlet) and energy consumed (effective work of compression). The kinetic energy of gas was used to power turbocharger, moreover the portion of mechanical energy from turbine shaft powered the mechanical compressor. Effective power of engine calculated from [Eq. (16)]:

$$N_e = \frac{L_e}{t_{cycle}} \tag{16}$$

where: N_e [W] – effective engine power, L_e [kJ] – effective engine work.
Energy efficiency of engine was calculated according to [Eq. (17)]:

$$\eta_E = \frac{L_e}{E_{chem}} \tag{17}$$

where: η_E [-] – energy efficiency of engine.

Specific fuel consumption calculated according to [Eq. (18)]:

$$g = \frac{l \cdot m_{pal} \cdot 1000 \cdot 3600}{t_{cykl} \cdot N_e} \tag{18}$$

The individual values of engine energy efficiency calculation are in Table 1.2.

Table 1.2. Energy efficiency calculation of presented engine concept

Type of energy	Value
Chemical energy of fuel	E_{chem}=2*0,0004278 kg*44600 kJ/kg=38,16 kJ
Effective work demand for turbocharger	$L_{eS\_turbospr}$=4,156 kJ
Effective work demand for compressor	L_{eS_spr}=4,456 kJ
Effective turbine work	L_{eT}=[(941Nm*32000rpm*0,0065s)/9549]*0,95 = 19,452 kJ
Effective work of rotating valve timing system	L_{eVTS}=[(837Nm*1538rpm*0,0065s)/9549]*0,95 = 0,832 kJ
Kinetic energy of gas at turbine outlet	$E_{k\_wyl\_turb}$=2,570 kJ
Effective work of engine	L_e=19,45+0,83+2,57-4,156-4,456=14,242 kJ
Effective power of engine	N_e=14,242kJ/0,0065s= 2191 kW
Energy efficiency of engine	η_E=14,242/38,16=0,373
Specific fuel consumption	g=2*0,0004278*1000*3600/(0,0065*2191) = 216,3 g/kWh

3. Conclusions

The turboshaft engine concept working according to the Humphrey cycle was presented. The engine operation requires the implementation of the following stages: preparation of high-pressure gases and supplying the turbine with these gases. The engine is therefore powered by pulses, unlike classic turbine engines,

which are supplied continuously. The implementation of pulse powering requires the use of the valve timing system. It is an important component of the presented engine concept, and it has a decisive impact on its effective work. The efficient operation of the engine according to Humphrey cycle was ensured by the innovative concept of a rotating valve timing system. It guarantees the continuity of flow in the nozzles, effective expansion of the exhaust gas through the nozzles with different ratios of the maximum cross-sectional area to the minimum cross-sectional area and optimal attack angles of the flowing gas to the turbine.

A very important advantage of the presented engine concept is its simple construction. It consists of six stationary combustion chambers, single component rotating valve timing system and one-stage turbine. In addition, engine operation is ensured by only rotation of rotating valve timing system. The valve timing system is a self-propelled. Its motion is caused by the jet force generated in the nozzles.

The presented engine concept stands out big energy efficiency (η_E = 0,373) and small specific fuel consumption (g = 216,3 g/kWh). The engine performance parameters are better than classical turboshaft presented at the beginning of the paper. The best of them Rolls-Royce Turbomeca RTM322 (1799 kW) has energy efficiency 0,321 and specific fuel consumption 261,8 g/kWh.

Presented performance parameters should be treated with some caution, because parameters of Turbomeca RTM322 are measured at engine test bench. The parameters of presented engine concept is result of numerical simulation. For obtained results it should be assumed that a margin of error is possible because:

- despite the use of advanced 3-dimensional numerical analysis and one of the best CFD software ANSYS Fluent, simulation is inherently some kind approximation of real physical phenomena. It is worth noting, however, that this approximation is the most accurate that can be calculated nowadays,
- simulation model of engine has not included heat losses form rotating valve timing system and from turbine. It would influence calculated parameters, however it is estimated that it would has small impact,
- assumed mechanical efficiency 0,95 for turbine and rotating valve timing system may vary in reality. Construction details are not designed yet,
- at the stage of the numerical prototyping, it is impossible to predict all the required design details of the engine. They can affect the final parameters of the engine.

A proper and final comparison of pulsed powered turbine engine with existing on the market engines can be realized only through its physical construction and measurement at engine test bench. If the performance parameters of presented engine concept confirmed, the presented concept of a pulsed power turbine engine would certainly be a competition for the turboshaft engine existing on the market.

The key issue seems to be ensuring proper sealing between the chambers and the rotating timing. In simulation perfect sealing was assumed.

To ensure efficient engine operation, the rotating nozzles should rotate at a precisely defined speed. This requirement should be implemented by using a rotation speed stabilizing system that simultaneously would accumulate the work done by the rotating valve timing system (for example, charging the batteries and driving the auxiliary equipment).

References

[1]. Balicki W. Korczewski Z., Szczecinski S. Obszary Zastosowań i Tendencje Rozwojowe Turbinowych Silników Spalinowych. SILNIKI SPALINOWE. 3, 2007.

[2]. Szlachetka M. Pietrykowski K., Magryta P. Badania symulacyjne bilansu cieplnego silnika Diesla przeznaczonego do napędu lekkiego śmigłowca. 2014.

[3]. Brophy, C., and G. Roy. 2009. "Benefits and challenges of pressure-gain combustion systems for gas turbines." Mech. Eng. 131 (3): 54–55. https://doi.org/10.1115/1.2009-MAR-8.

[4]. Ostapski W. Wierzchnoń T., Rudnicki J., Dowkontt S. Simulation and Bench Studies of the Constructively and Technologically Modernized High Performance Piston Aircraft Engine. Stage I. Bulletin of the Polish Academy of Sciences. 2017.

[5]. Ostapski W. Analysis of thermo-chemical response in and aircraft piston engine by analytical, FEM, and test-stand investigations. Journal of Thermal Stress. 2011.

[6]. General Electric T700. Wikipedia. [Online] [Cited: 23 09 2017.] https://en.wikipedia.org/wiki/General_Electric_T700.

[7]. Engines Gas Turbine. Aviation week and space technology, January 2008. [Online] http://www.geocities.jp/nomonomo2007 /AircraftDatabase/AWdata/AviationWeekPages/GTEnginesAWJan2008.pdf..

[8]. Richards G.A. New Developments in Combustion Technology Part II: Step change in efficiency. 2012.

[9]. Akbari P. Nalim M.R. Review of Recent Developments in Wave Rotor Combustion Technology. Journal of Propulsion and Power. 2009, Tom 25, 4.

[10]. Akbari P. Nalim M.R., Mueller N. A Review of Wave Rotor Technology and Its Application. Journal of Engineering for Gas Turbines and Power. 2006, Tom 128. https://doi.org/10.1115/1.2204628

[11]. Piechna J. Micro Ring-Engine Numerical Fluid Dynamics Analysis. Proceedings of PowerMEMS . 2008.

[12]. Kurec K. Piechna J., Müller N. Numerical investigation of the micro radial disk internal combustion engine. Archivum Combustionis. 2014, strony No 1, pp 1-25.

[13]. Vagani M. Pohorelsky L., Sun G., Alemu D., Lee J.R., Kelly R.T., Qualman T.J. A Wave Disc Engine Concept For Micro Power Generation.

[14]. DORI J. KLINAR van I.J. Efficiency Characteristics of a New Quasi Constant Volume Combustion Spark Ingnition Engine.pdf. Thermal Science. 1, 2012, Tom 17.

[15]. Piechan J. Łapiński D. Improvemenets in the turbo-engine by replacement of conventional combustion chamber by pulse combustion chamber. Archive of Mechanical Engineering. 2013.

[16]. Szargut J. *Termodynamika techniczna* [Technical thermodynamics]. Warsaw, Poland: Wydawnictwo Naukowe PWN, 1991. ISBN 83-01-10104-0.
[17]. Holzwarth H. Junghans E. Improvements in Gas Turbines,. "U.K. Patent No. 20, 546. 1906.
[18]. Griepe A. Gas Turbine-Engine. U.S. Patent No. 910, 665. 1909.
[19]. Lutoschkin E. Pressure-Gain Combustion for Gas Turbines Based on Shock-Flame Interaction. Doctoral dissertation, University of Stuttgar. 2014.
[20]. Hagen H. Constant Volume Combustion Gas Turbine with Intermittent Flows. U.S. Patent No. 3, 877, 219, . 1975.
[21]. Gertz A. Gas Turbine Engine. U.S. Patent No. 4, 241, 576. 1980.
[22]. Labarrere, L., T. Poinsot, A. Dauptain, F. Duchaine, M. Bellenoue, and B. Boust. 2016. "Experimental and numerical study of cyclic variations in a constant volume combustion chamber." Combust. Flame 172:49–61. https://doi.org/10.1016/j.combustflame.2016.06.027.
[23]. Tarnawski P. Ostapski W. Pulse Powered Turbine Engine Concept – Numerical Analysis of Influence of Different Valve Timing Concepts on Thermodynamic Performance. Bulletin of the Polish Academy of Sciences. 2018 No 3 June. https://doi.org/10.24425/123444
[24]. Tarnawski P. Analytical Performance Evaluation of Humphrey Cycle for Turbine Engine Application. Machine Dynamics Research. Vol. 41, No 3, 27-37.
[25]. Tarnawski P. Ostapski W. Pulse Powered Turbine Engine Concept Implementing Rotating Nozzles – Numerical CFD Analysis. Journal of Aerospace Engineering. 2019 July No. 3. DOI: 10.1061/(ASCE)AS.1943-5525.0001001
[26]. Tarnawski Piotr. Kncepcja silnika turbinowego o zasilaniu pulsacyjnym. Doctoral dissertation – Warsaw University of technology 2018.
[27]. Derlukiewicz D. Metoda Modelowania Zjawisk Termosprężystych w Warstwowych Powłokach Ceramicznych. Doctoral dissertation, Wrocław University of technology 2006.
[28]. Zdvorak E. H. Constant Volume Combustion Turbine with Plurality Flow Turbine Wheels. 1998.

Chapter 3.

Andrzej CHMIELOWIEC[1]

IMPLEMENTATION OF THE MOUNTAIN CLUSTERING METHOD AND COMMENTS ON ITS PRACTICAL USE FOR DETERMINING CLUSTER CENTRES

Abstract

For certain applications a need arises to reduce a large set of measurement data and select a group of the most representative data. Such a situation occurs for example in the case of the fuzzy logic algorithms whose computational complexity makes them inapplicable to too large input sets. One of the methods to reduce a data set is to determine the centre of clusters, that is the elements being the optimum representation of the entire set. The purpose of this paper is to describe the operation of the potential method designed to locate the centres of clusters in the entire set of measurement data. We present the selection algorithm based on the assumption that in certain local environments data are normally distributed. This assumption proves to be correct in numerous practical applications; however, in some cases a different probability distribution may seem more appropriate. For these cases we will only hint at how one can try to modify the potential function to produce the most reliable effect. Along with the mathematical description of the method we also present the functionality of a dedicated software implemented for this purpose.

Keywords:
statistics, data analysis, measurement data processing, cluster estimation, software for cluster estimation

1. Introduction

Over the recent years, methods of acquiring large quantities of measurement data have developed significantly. The processing of ever larger data sets poses a major challenge for statistical analysis, inference and machine learning

[1*] Faculty of Mechanics and Technology, Rzeszow University of Technology, al. Powstańców Warszawy 12, 35-959 Rzeszów, Poland, e-mail: achmie@prz.edu.pl

algorithms. One approach assumes that enormous data sets are partitioned into subsets called clusters represented by individual elements - cluster centres.

Section two presents the mountain clustering method designed to locate cluster centres. Section three discusses how this method is linked with statistics and probability, and provides guidelines on how to prepare measurement data properly. Finally, section four presents the results of the author's implementation of the subtractive mountain clustering method.

2. Mountain Clustering

Proposed by Yager and Filev [27, 28, 29], mountain clustering is one of the best methods to divide a set into a certain number of clusters/subsets. However, in order to create specific subsets, it is necessary to locate the so-called cluster centres. In general, any point of the measured space can be a cluster centre. Such an approach, however, results in computationally intensive algorithms of exponential complexity. The subtractive mountain clustering method [7], developed by Chiu and discussed in this article, takes a slightly different direction. It assumes that only an element of a set of data points can be a cluster centre. Thus, the method proposed by Chiu determines the starting points of clusters made up of a single point being the first element of a subset. Under the subtractive mountain clustering method, the searched space is limited to a divided set of points. However, due to its quadratic complexity with respect to the number of elements of a set, it is only used for medium-size sets [10].

The idea of subtractive mountain clustering is to determine function P for each point x_i representing its potential. It is therefore assumed that the potential in the i-th point of a set is given by

$$P(i) = \sum_{j=1}^{N} e^{-\alpha \left\| x_i - x_j \right\|^2}, \tag{1}$$

for $i = 1, \ldots, N$, and $\alpha = 4 / (r_a)^2$ for constant $r_a > 0$. The form of the mountain function clearly shows that a data point with more neighbouring data points will have a higher potential value. This property makes subtractive mountain clustering much more resistant to disturbances caused by the emergence of random points compared with other clustering algorithms, such as C-means [17, 15] and FCM [4, 5, 6, 11].

After computing potential $P(i)$ of every data point, the data point with the highest potential is selected as the first cluster centre. Consequently, $c_1 = x_u$, where $u = \arg_i \max P(i)$, and $P(u)$ is given by P^* and is assumed to be the reference potential for the selection of new cluster centres. In addition, each time we select the next centre of the next cluster $c_k = x_u$ (for the relevant u), we revise the value of the mountain function assigned to particular points of a set in the following manner

$$P(i) = P(i) - P(u)e^{-\beta\|x_i - c_k\|^2}, \quad (2)$$

where $\beta = 4 / (r_b)^2$ for $r_b > 0$ is a constant defining the range of the mountain function. For the sake of practicality, we assume that $r_b > r_a$ and most often $r_b = 1.25\ r_a$. We continue to estimate new cluster centres until the potential of all points exceeds threshold $\varepsilon_d P^*$ for ε_d selected from range (0, 1).

The following algorithm presents how subtractive mountain clustering works [7, 8].

1. Select r_a,, r_b,, ε_u and ε_d.
2. Compute potential $P(i)$ of every point from set ($i = 1, \ldots, N$).
3. Select point x_u with the highest potential $P_u = P^*$ as the first cluster centre.
4. Assume that $k = 2$.
5. Then, keep repeating the following steps:
    a) Select point x_u with the highest potential P_u.
    b) If $P_u > \varepsilon_u P^*$, then x_u becomes the centre of the k-th cluster. If $\varepsilon_u P^* > P_u > \varepsilon_d P^*$, then x_u becomes centre c_k of the k-th cluster if it meets additional criteria (depending on how the algorithm is implemented).
    c) Assume that $k = k+1$.
    d) If $P_u > \varepsilon_d P^*$, end the clustering process - there are no more cluster centres.

Subtractive mountain clustering can be improved by incorporating a search by different values of α and β parameters. This way we obtain a least biased method [3]. We can even try to come up with a result similar to that produced by methods designed to estimate clusters with the lowest possible entropy [21, 20]. In addition, it is possible to replace the Gaussian potential function with the first-order Cauchy function [1]. A modified mountain function may also be used to estimate other types of clusters, for example circular shells [18]. If we add to that the option to replace the Euclidean distance with a kernel-induced distance [14], it turns out that subtractive mounting clustering is highly useful for estimating clusters in a given set.

The cluster centres determined using subtractive mountain clustering can be used to establish fuzzy inference rules for the purpose of various artificial intelligence algorithms [1, 19, 22, 23, 24]. In particular, they can be used to develop models predicting the behavior of various types of complex systems over time [16, 12, 9, 13], or in other words, to create machine learning algorithms.

3. Links of mountain clustering with statistics and probability

Let us now determine the relationship between equation (1) and the classical theory of probability. First, note that the mountain function is very similar to the probability density function for a normal distribution, which for $\mu = 0$ is given by

$$\Phi(x) = \frac{1}{\sigma\sqrt{2\pi}} \exp\left(-\frac{x^2}{2\sigma^2}\right). \quad (3)$$

Taking into account the values of mountain function *P,* we can see that the following approximation is true

$$\exp(-\alpha x^2) = \exp\left(-\frac{4x^2}{r_a^2}\right) = \exp\left(-\frac{\frac{8}{9}x^2}{2(r_a/3)^2}\right) \cong \exp\left(-\frac{x^2}{2(r_a/3)^2}\right). \quad (4)$$

This means that r_a corresponds to approximately three standard deviations σ of a normal distribution presented in Figure 3.1. This interpretation of the mountain function means that clusters are in fact subsets of points concentrated around the centres according to a normal distribution with a given standard deviation. This correspondence would be accurate, if parameter α was defined as 4.5 / $(r_a)^2$.

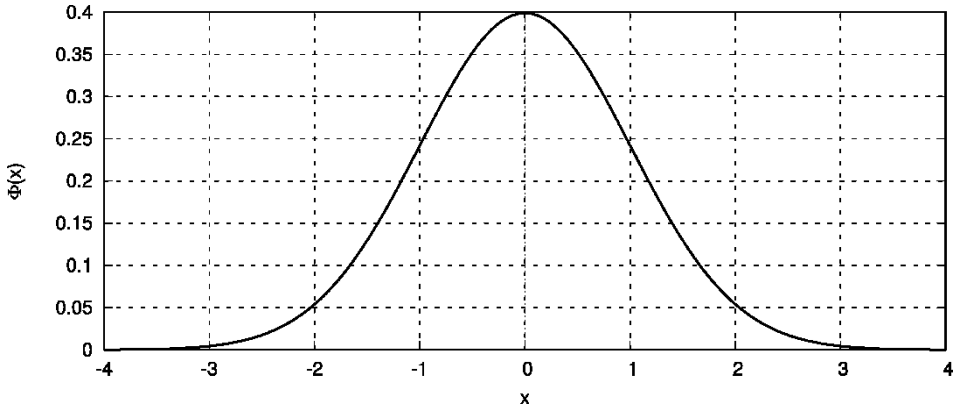

Fig. 3.1. Normal distribution curve for $\mu = 0$, $\sigma = 1$

Now, it is easy to imagine that the Gaussian mountain function is replaced with another continuous probability distribution. This way we can better match the division into clusters in terms of points having a different probability distribution on individual coordinates. We can even try to define the mountain function for each coordinate of a point separately.

Another major conclusion from the above observations is that we can attempt to replace values $\|x_i - x_j\|$ with any other metric - not necessarily the Euclidean distance. Speaking of metrics, we must emphasize how important the process of normalizing coordinates of a point is to subtractive mountain clustering. If points x_i have only one coordinate, then normalization does not affect the results obtained. However, if points x_i have two or more coordinates, a failure to normalize individual coordinates may result in there being only one coordinate

significantly affecting the final result. For example, let us imagine that the values of the first coordinate are from range [0, 1] and the values of the second coordinate are from range [99, 100]. It is not difficult to find such examples in the measuring practice. Note that, in principle, only the second coordinate having high absolute values has any significant effect on the value of the mountain function. That is why, before employing subtractive mountain clustering, it is important to scale down the values of each coordinate and move them, for example, to variability range [0, 1]. Then, the weight of each coordinate of a point will be identical and will have the same effect on the value of the mountain function.

4. Application for Estimating Cluster Centres

The subtractive mountain clustering algorithm has been implemented in the form of a browser application with graphical presentation of results. The implementation is available for download from the author's website: https://achmie.v.prz.edu.pl/materialy-do-pobrania/materialy-ogolnodostepne/mountain-clustering-3.html

Figure 3.2 shows the result produced in the application for a sample set of 200 data points with three coordinates. The individual stages of determining the subsequent cluster centres are presented in Figure 3.5 at the end of the article.

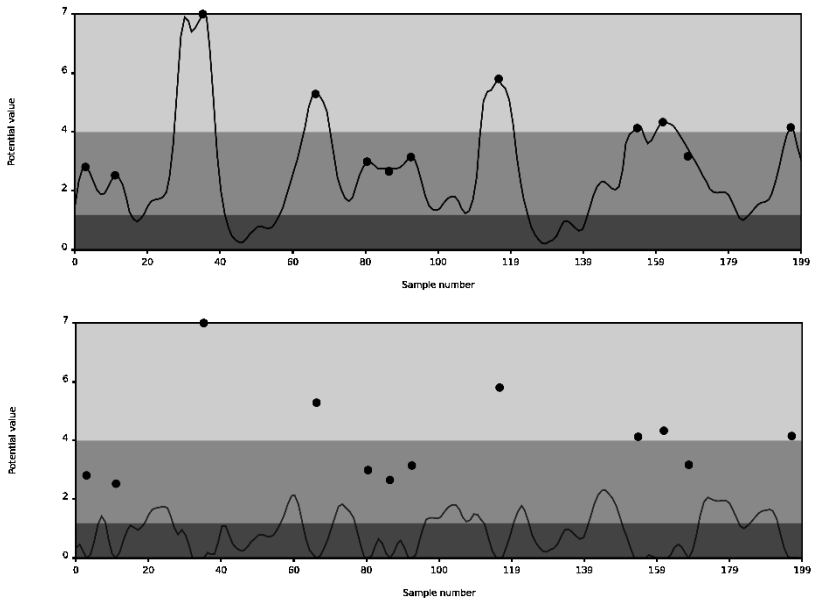

a)

b)

Fig. 3.2. Values of the mountain function for a sample of 200 three-dimensional points: a) values of the mountain function when the algorithm starts to run, b) values of the mountain function after all cluster centres have been located

In order to illustrate how the implemented method works, a version of the application dedicated exclusively to two-dimensional data has been developed. Its main purpose is to show the readers what cluster centres should really be.

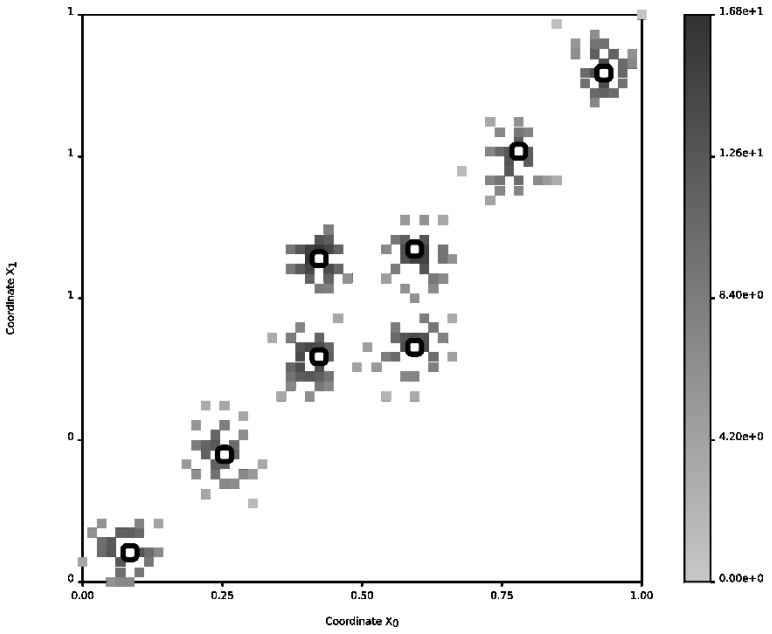

Fig. 3.3. The cluster centres located in the centres of individual clusters of points - the effect of a proper selection of radiuses $r_a = 0.10$ and $r_b = 0.14$

Figure 3.3 is a perfect illustration of the above. It shows that for well-chosen parameters r_a and r_b cluster centres should occur more or less in the centres of clusters of points. For poorly chosen parameters there may be too many or too few cluster centres as shown in Figures 3.4 a) and 4 b) respectively. Proper selection of these parameters is impossible without a thorough knowledge of the measurement data. These parameters can be, for example, in close correlation with certain settings and properties of the measuring device or may be related to the statistical distribution of a given coordinate. The two-dimensional version of the application features a button making it possible to disable normalization of the coordinates used in individual measurements. This allows us to check how much the results of this method depend on the absolute values of coordinates (as mentioned in the previous section).

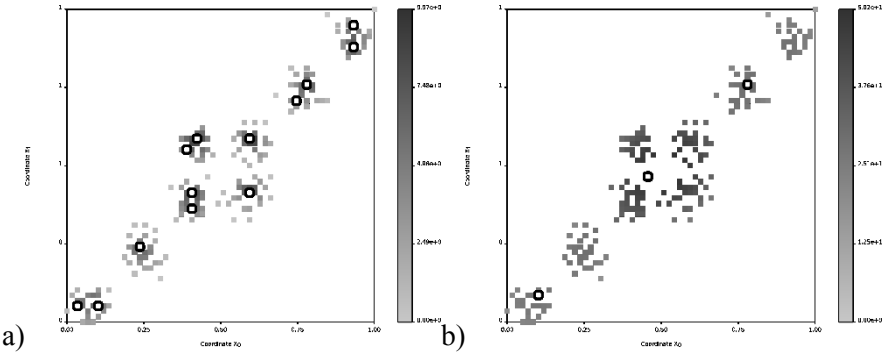

Fig. 3.4. Cluster centres located too densely and too sparsely due to poor choice of radiuses: a) too densely for $r_a = 0.06$ and $r_b = 0.08$, b) too sparsely for $r_a = 0.28$ and $r_b = 0.36$

5. Conclusions

The article proposes a practical approach to subtractive mountain clustering and presents an IT tool designed for its implementation. Sections three and four discuss practical issues related to the proper use of the method in question. In particular, special attention is paid to the need to normalize all coordinates before starting the clustering process. The second important conclusion is drawn from the practical examples showing how the final results are influenced by poor choice of input parameters such as r_a and r_b.

The study was carried out with the use of apparatus purchased from funds of the project 'Establishment of the Scientific and Research Inter-University Laboratory in Stalowa Wola', realized as part of the Operational Programme Eastern Poland 2007–2013, Priority axis I 'Modern Economy', Measure 1.3 'Supporting Innovativeness' as per contract No. POPW.01.03.00-18-016/12-00.

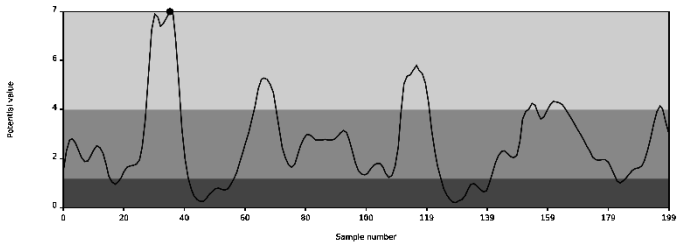

a)

b)

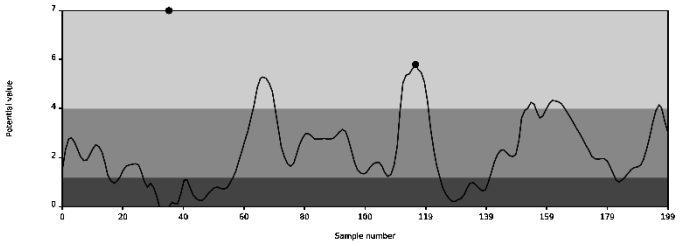
Pgcentsi value
Sample number

c)

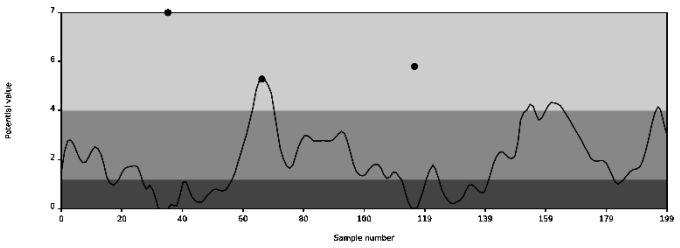
Pgcentsi value
Sample number

d)

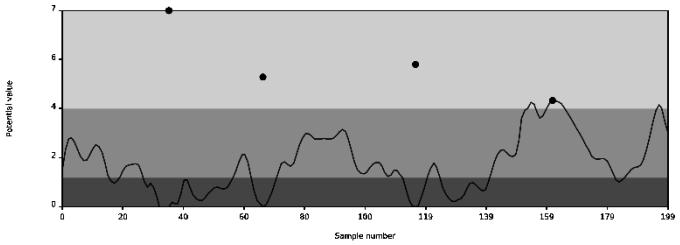
Pgcentsi value
Sample number

e)

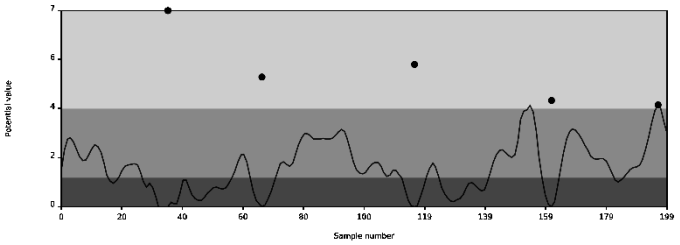
Pgcentsi value
Sample number

f)

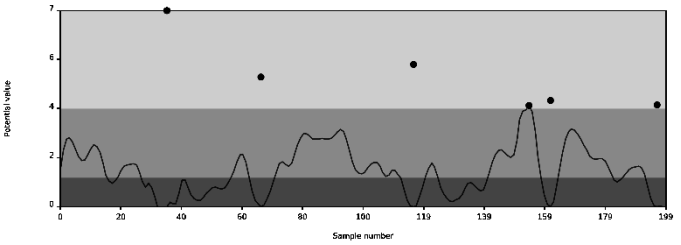
Pgcentsi value
Sample number

g)

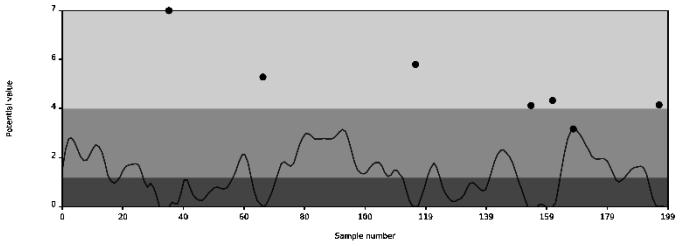
Potential value
Sample number

h)

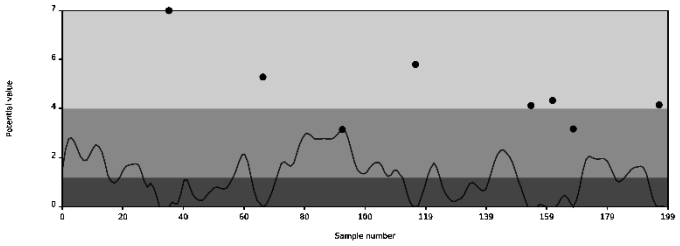
Potential value
Sample number

i)

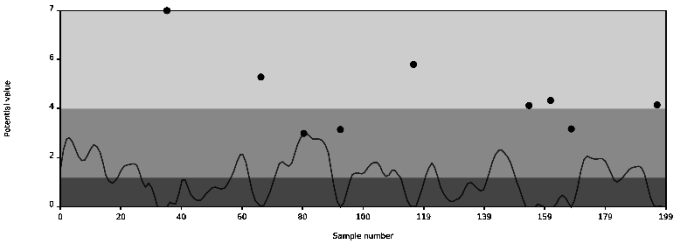
Potential value
Sample number

j)

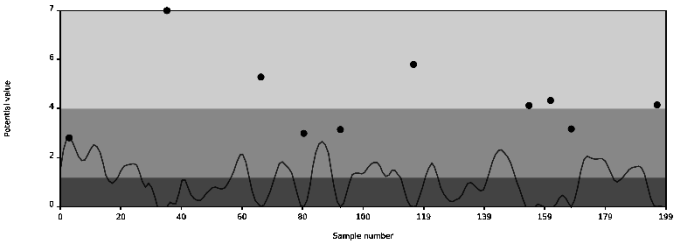
Potential value
Sample number

k)

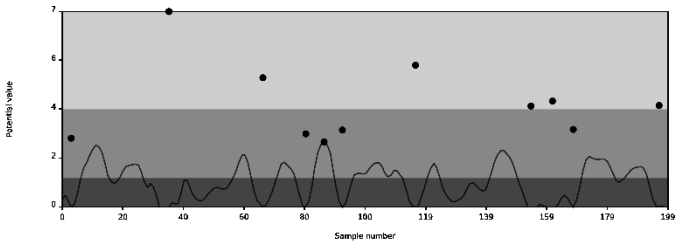
Potential value
Sample number

l)

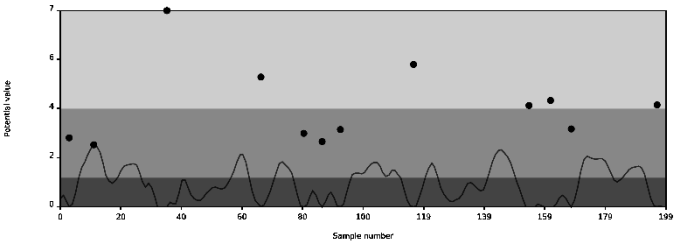

m)

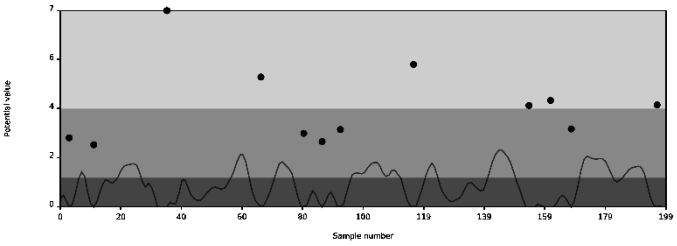

Fig. 3.5. Subsequent steps of the subtractive mountain clustering method on the example of a sample set of 200 three-dimensional data points; letters from a) to m) mark figures showing the modified mountain function curves and selected cluster centres

References

[1] Angelov P.P., Filev D.P. (2004). An approach to online identification of Takagi-Sugeno fuzzy models. IEEE Trans. Syst. Man. Cybern. Vol. 34(1). pp. 484-498.

[2] Astrom K.J., Wittenmark B. (1984). Computer Controlled Systems: Theory and Design, Prentice Hall Professional Technical Reference.

[3] Beni G., Liu X. (1994). A least biased fuzzy clustering method. IEEE Trans. Pattern. Anal. Mach. Intell. Vol. 16(9). pp. 954-960.

[4] Bezdek J. (1974). Cluster validity with fuzzy sets. J. Cybernetics. Vol. 3(3). pp. 58-71.

[5] Bezdek J. (1981). Pattern recognition with fuzzy objective function algorithms. Plenum Press, New York.

[6] Bezdek J., Hathaway R., Sabin M., Tucker W. (1987). Convergence theory for fuzzy c-means: Counterexamples and repairs. The Analysis of Fuzzy Information, Bezdek J. (ed), CRC Press, Vol. 3, Chap. 8.

[7] Chiu S.L. (1994). Fuzzy model identification based on cluster estimation. J. Intell. Fuzzy Syst. Vol. 2(3). pp. 267-278.

[8] Chiu S.L. (1994). A cluster estimation method with extension to fuzzy model identification. In: Proc IEEE Int. Conf. Fuzzy Syst., Orlando, FL, Vol. 2. pp. 1240-1245.

[9] Crowder R.S. (1990). Predicting the Mackey-Glass time series with cascade-correlation learning. In Proc. 1990 Connectionist Models Summer School, Carnegie Mellon University, pp. 117-123.

[10] Dave R.N., Krishnapuram R. (1997) Robust clustering methods: A unified view. IEEE Trans. Fuzzy Syst. Vol. 5(2). pp. 270-293.

[11] Dunn J. (1974). A fuzzy relative of the ISODATA process and its use in detecting compact, well separated cluster. J. Cybernetics. Vol. 3(3). pp. 32-57.
[12] Jang J.S.R. (1993). ANFIS: Adaptive-network-based fuzzy inference system. IEEE Trans. on Systems, Man. & Cybernetics. Vol. 23(3). pp. 665-685.
[13] Kikuchi S., Nanda R., Perincherry V. (1994). Estimation of trip generation using the fuzzy regression method. 1994 Annual Meeting of Transportation Research Board, Washington, D.C.
[14] Kim D.W., Lee K.Y., Lee D., Lee K.H. (2005). A kernel-based subtractive clustering method. Pattern Recogn. Lett. Vol. 26. pp. 879-891.
[15] Linde Y., Buzo A., Gray R.M. (1980). An algorithm for vector quantizer design. IEEE Trans. Commun. Vol. 28. pp. 84-95.
[16] Mackey M., Glass L. (1977). Oscillation and chaos in physiological control systems. Science. Vol. 197. pp. 287-289.
[17] MacQueen J.B. (1967). Some methods for classification and analysis of multivariate observations. In: Proc 5th Berkeley Symp on Math Statistics and Probability, University of California Press, Berkeley, pp. 281-297.
[18] Pal N.R., Chakraborty D. (2000). Mountain and subtractive clustering method: Improvements and generalizations. Int. J. Intell. Syst. Vol. 15. pp. 329-341.
[19] Powell M.J.D. (1987). Radial basis functions for multivariable interpolation: a review, Algorithms for approximation, Clarendon Press, New York, NY.
[20] Rose K. (1998). Deterministic annealing for clustering, compression, classification, regression, and related optimization problems. Proc. IEEE. Vol. 86(11). pp. 2210-2239.
[21] Rose K., Gurewitz E., Fox G.C. (1990). A deterministic annealing approach to clustering. Pattern Recogn. Lett. Vol. 11(9). pp. 589-594.
[22] Strobach P. (1990). Linear Prediction Theory: A Mathematical Basis for Adaptive Systems, Springer-Verlag New York, Inc., Secaucus, NJ.
[23] Sugeno M., Tanaka K. (1991). Successive identification of a fuzzy model and its applications to prediction of a complex system, Fuzzy Sets and Systems, Vol. 42(3), pp. 315-334.
[24] Takagi T., Sugeno M. (1985). Fuzzy identification of systems and its application to modeling and control. IEEE Trans. on Systems, Man. & Cybernetics. Vol. 15. pp. 116-132.
[25] Wang L.X., Mendel J.M. (1992). Generating fuzzy rules by learning from example. IEEE Trans. on Systems, Man. & Cybernetics. Vol. 22(6).
[26] Wang L.X. (1993). Training of fuzzy logic systems using nearest neighborhood clustering. Proc. 2nd IEEE Int. Conf. on Fuzzy Systems (FUZZ-IEEE). pp. 13-17.
[27] Yager R.R., Filev D.P. (1993). Learning of fuzzy rules by mountain clustering. Proc. SPIE Conf. on Applications of Fuzzy Logic Technology. pp. 246-254.
[28] Yager R.R., Filev D.P. (1994). Generation of fuzzy rules by mountain clustering. J. Intell. Fuzzy Syst. Vol. 2(3). pp. 209-219.
[29] Yager R.R., Filev D.P. (1994). Approximate clustering via the mountain method. IEEE Trans. Syst. Man. Cybern. Vol. 24(8). 1279-1284.

Chapter 4.

Krzysztof NOZDRZYKOWSKI[1*]
Sławomir JASZCZAK[1]

THE FORCE VALUE CONTROL IN THE CRANKSHAFT FLEXIBLE SUPPORT SYSTEM

Abstract

The article presents an original, innovative solution of the measurement system designed for the assessment of the condition of large crankshafts. The basic components of the system are described, particularly the flexible support system, composed of a set of supports, whose function is to adjust the set values of support reaction forces eliminating deflection and elastic deformations of the tested object that occur under the weight of the rotating crankshaft. The functional structure of the support control system and the algorithms of denoising the measurement signals and stabilizing the values of the applied reaction forces. The example results of the tests make up the basis for final conclusions.

Keywords:
Control, force value, flexible suport, measurement, crankshaft.

1. Introduction

The correct assessment of the geometrical state of very large crankshafts depends on the conditions of measurement itself, in particular on effective elimination of elastic deformations of the crankshaft caused by its own weight [1, 2, 3, 4]. As shown in the works [5, 6], these conditions can be provided by resting the crankshaft's main journals by a set of supports that will exert specific variable reaction forces at the support head-journal interface. The diagram of the measurement system (Fig. 4.1) equipped with a set of supports eliminating the elastic deflection and deformations induced by the crankshaft weight consists of four components, or systems:

- flexible support,
- measurement,
- crankshaft rotation,
- data processing and analysis.

[1] Institute of Basic Technical Sciences, Faculty of Marine Engineering, Maritime University of Szczecin, Willowa 2-4, 70-500 Szczecin, Poland;
* k.nozdrzykowski@am.szczecin.pl

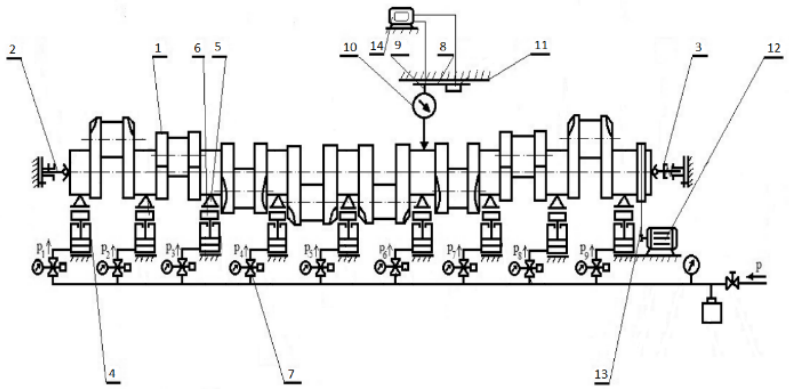

Fig. 4.1. The schematic diagram of the essential elements of the measurement system [5, 6]: 1 - crankshaft, 2 and 3 - locating centre points, 4 - support with a pneumatic actuator, 5 - V-block head, 6 - force sensor, 7 - precision current-controlled valve, 8 - carriage, 9 - stand, 10 - measuring sensor, 11 - guides, 12 – geared motor, 13 - belt transmission, 14 - PC and software

The flexible support system is formed by a set of pneumatic supports 4, fitted with V-block heads 5, force sensors 6 and precision controllable valves 7. The measurement system consists of a carriage 8, a stand 9 mounted on the carriage and a measuring sensor 10, moving clearance-free along the crankshaft on precision guides 11. The drive turning the measured crankshaft 1 consists of a geared motor 12 and belt transmission 13, while a PC computer 14 with software make up the data processing and analysis system.

2. Stabilization of the signal and the dynamics of control unit operation

Flexible supports, constructed as shown in Figure 4.2, are fitted with self-aligning, rolling, articulated V-block heads that in connection with pneumatic actuators execute all degrees of freedom. The supports are elements exerting passive reaction force applied in order to eliminate elastic deflections of the shaft under its own weight. At the same time, they compensate possible displacements caused by geometric deviations.

Fig. 4.2. A complete flexible support with a force sensor and a controllable valve [5, 6]

One of the essential elements of the flexible support system, responsible for the implementation of the set values of the reaction forces is the control and monitoring unit. Whether the set values are correctly executed by the control unit largely depends on the stabilization of the control signal.

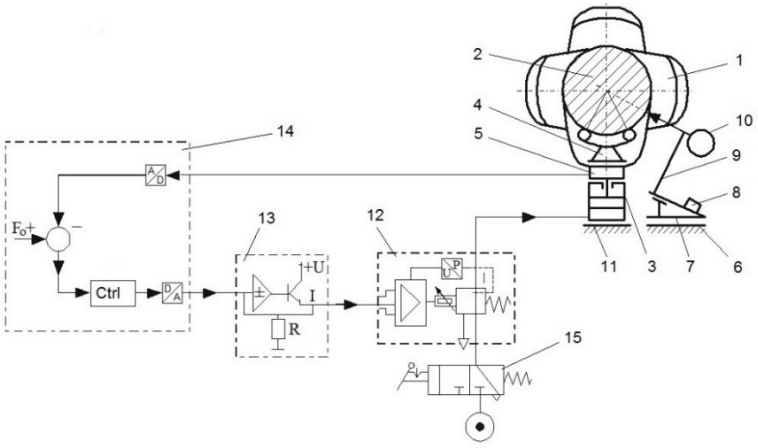

Fig. 4.3. Basic elements of the flexible support control unit [5, 6]:
1 – crankshaft, 2 – shaft's main journal, 3 – pneumatic actuator, 4 – rolling, articulated, self-adjusting vee-block head, 5 – force sensor (force transducer), 6 – guides, 7 – trolley, 8 – laser distance meter for measuring the longitudinal coordinate of the measured cross-section, 9 – tripod, 10 – sensor for measuring geometric deviations, 11 – base, 12 – proportional current-controlled reducing valve (controlled proportional regulating valve), 13 – current relay, 14 – programmable digital controller (control circuit), 15 – feed valve, A – analogue signal, Ctrl – controller, D – digital signal, Fo – signal of the set force, I – current signal, P – pressure, R – resistance, U – voltage

Figure 4.3 presents a general diagram of the unit controlling the reaction force of the flexible support. The basic part of the control unit is the programmable digital controller (X20CP1586), usually used in industrial automation systems. The controller co-operates with the system via input/output devices, digital/analog and analog/digital units.

The functional structure of the force control unit is shown in Figure 4.4. The main function of the control unit is to ensure that the force FPV (t) is stable and approximately the same as the set FSP (t). The list of all physical variables in the control system is given in Table 4.1. The input force FPV (t), reaction force at the interface of the head and the main bearing journal, is measured by the force transducer and put into the control unit through an analog module (X20AI4632). The set reaction force is exerted by the pneumatic actuator with a pressure regulator (PRE-I2) that acts as an analog device. An analog control signal UI (t) activates the pneumatic actuator based on the module of analog outputs (X20AO4622) and a pressure regulator. The pneumatic cylinder produces an effective manipulated signal, i.e. the force applied to the main journal of the crankshaft. The algorithm for continuous PID control has been used at the output for controlling the signal of the set reaction force in the crankshaft flexible support system.

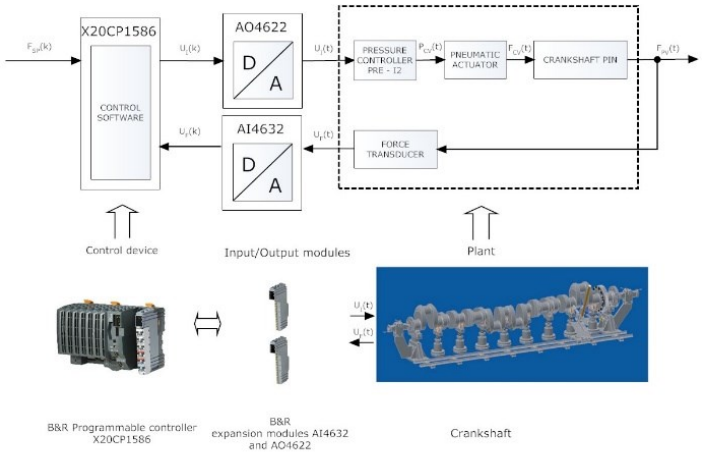

Fig. 4.4. The structure of crankshaft force control system [prepared by the author]

Table 4.1. List of physical variables in the force control unit signal description range unit

signal	description	range	unit
FSP (t)	value corresponding to the set force	0-2000	N
FPV (t)	value corresponding to the current force.	0-2000	N
PCV(t)	value corresponding to the pressure signal	0-2000	mbar

However, in this case the signal from the force transducer showed relatively high noise resulting, inter alia, from high sensitivity of the measuring instrument and susceptability to external factors (vibrations). The mean noise amplitude was 40 ÷ 60 N. Figure 4.5 depicts changes in the force signal value set at 907 N, where an output algorithm of force setpoint control was used.

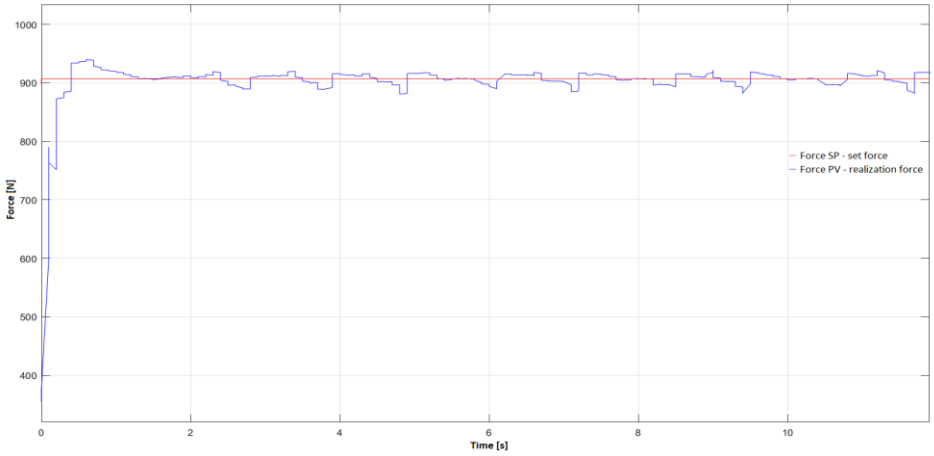

Fig. 4.5. Changes in the setpoint force of 907 N with the use of an output algorithm for controlling the set reaction force [prepared by the author]

From the practical viewpoint, the use of force transducers of such performance in industry can be considered as typical and insignificant for the execution of the specific task. High sensitivity of the extensometers used in force transducers leads to fluctuations of the measuring signal, and further to the fluctuations of the control signal and difficult operation of the executive systems, i.e. the necessity of frequent switching. The application of such transducers for the execution of the set force in the control system under consideration required that the control signal fluctuations be minimized. Therefore, a filtration module has also been used in the force control algorithm. The moving average filter has been used, as indicated in Fig. 4.6 and formula (1), that generates the continuously updated

average value of the input x by using the previous number of cycles, defined in the base, and conveys it to the output y, [7, 8].

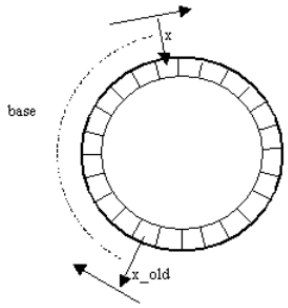

Fig. 4.6. General concept of the moving average filter [7]

$$y = \frac{sum\_old - x\_old + x}{base}$$
$$sum\_old = sum\_old - x\_old + x \quad (1)$$

where: sum_old – sum of the values of signal x samples,
base_– number of signal x samples for adding up (averaging base),
x – value of the current signal sample,
x_old – value of the historical sample at a distance equal to the base,
y – averaged value of signal x.

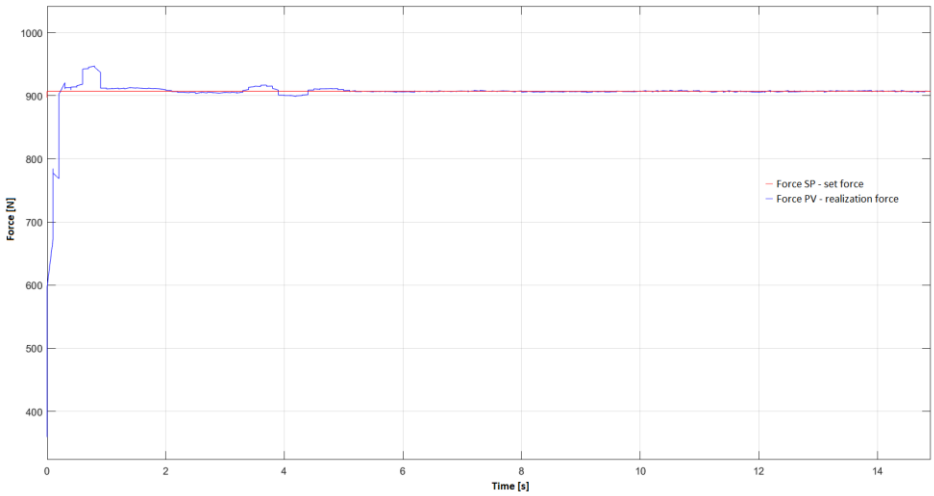

Fig. 4.7. Changes in the setpoint force of 907 N with the use of a moving average filter [prepared by the author]

After a moving average filter had been used, the noise amplitude dropped to a value of 4÷5 N, that can be regarded as sufficient for the execution of the assumed task. Figure 4.7 shows changes in the filtered signal for a set force value of 907 N.

A similarly essential issue for the control of the reaction force is the characteristic of the control unit dynamics, i.e. the speed of the response of the setting system (actuator) to the set pulse of the execution system (precision current-controlled valve).

The PID controller used, assuming ideal differentiation, implements the following algorithm, [9]:

$$u(t) = K_p\left(e(t) + \frac{1}{T_i}\int_0^t e(t)\,dt + T_d\frac{de}{dt}\right) \tag{2}$$

where :

e(t), u(t) – respectively: input signal (error signal) and output (control) signal of the controller,

Kp – gain,

Ti – time of doubling, or integration,

Td – time of advance (differentiation).

An increase in Kp accelerates the operation of the control system, but increases the overshoot Mp. Increased Ti slows down the control system operation, but reduces the overshoot Mp.

The basic quality indicators related to the response of the control systems of oscillating and non-oscillating nature to a unit step of the set variable are as follows: maximum dynamic error emax = max (e(t)) and dynamic deviations (related to the transient phase), i.e. overshoot Mp, rise time Tn and time of control Tr, Fig. 4.8 [9].

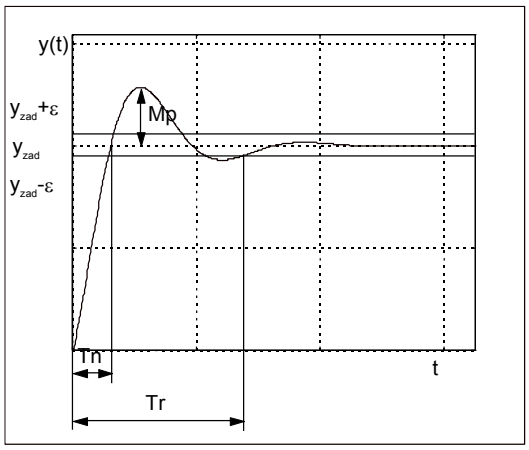

Fig. 4.8. Method of the determination of sectional quality indicators [9]

For the executed task, it is important that the change in control signal values is achieved at the minimized value of the overshoot. This reduces the impact of the dynamic elements of the control unit on the measurements of the geometric deviations of crankshafts. The minimization of the overshoot value is also recommended from practical point of view. In such cases there is a lower risk of exceeding allowable technological limits of the actuators and the control object itself, because excessive overshoot may result in the system failure or its total destruction.

Having regard to the above, a number of tests have been conducted to determine the dynamic characteristics of the control unit with the quality indicators optimal for the task performance. Thus, with the dynamic properties of the control unit maintained, the time of response to the set pulse of the actuator will be the shortest.

The dynamic characteristics of the control unit work show significant overshoot values when the reaction force value is changed by 5 N, in the range 897÷957 N, see Fig. 4.9. The characteristics shown in previous Figures 4.5 and 2.7 have similar changes of the force.

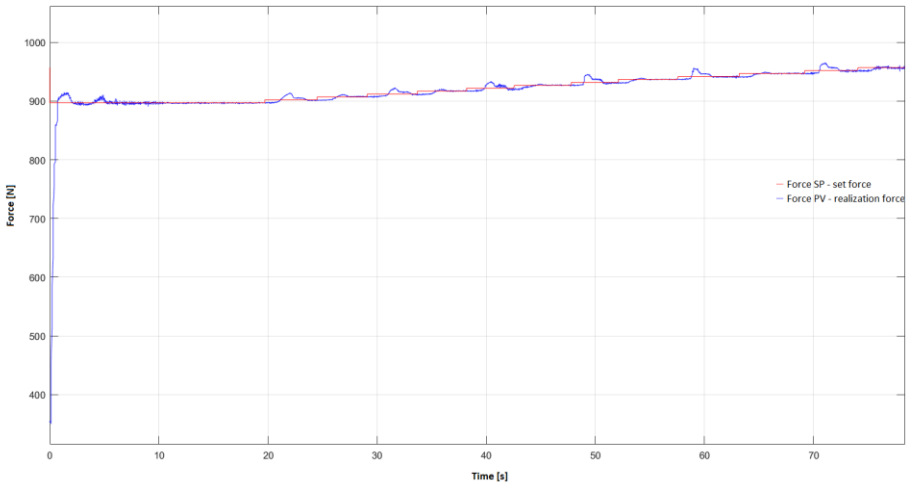

Fig. 4.9. Characteristic of the control unit work dynamics at a change in the value of the set reaction force every 5 N, in the range 897÷957 N, showing significant overshoot values [prepared by the author]

Figure 4.10 shows the control unit work dynamics at a change in the value of the set reaction force every 5 N, in the range 897÷957 N with experimentally determined quality indicators, optimal for the execution of the assumed task.

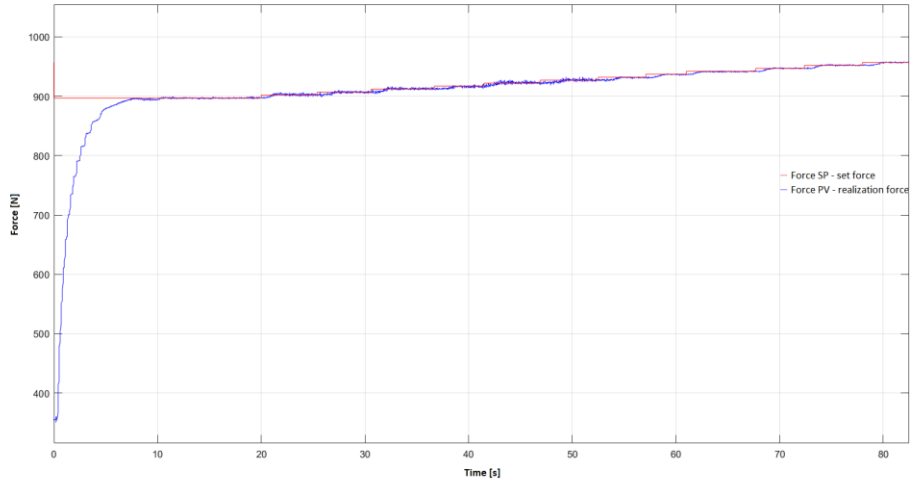

Fig. 4.10. Characteristic of the control unit work dynamics at a change in the value of the set reaction force every 5 N, in the range 897÷957 N, with the best quality indicators for the execution of the assumed task [prepared by the author]

3. Summary

The conducted tests, whose example results are presented in this article, have enabled the determination of the best parameters of the signal controlling the set value of the reaction force in the crankshaft flexible support system. The flexible support system is an important element of the measurement system intended for the assessment of the geometric deviations of the large-scale crankshafts. The application of the flexible support system enables, by appropriate control of the reaction forces of the supports, eliminating deflections and elastic deformations of the measured object caused by the crankshaft weight itself. Thanks to this solution, measurements can be taken in conditions corresponding to non-reference measurements when the crankshaft is fixed in centre points. One of the essential advantages of the control unit is its mild and stable characteristics of work dynamics, resulting in negligibly minor impact of the support conditions on the measurements of geometric dimensions

References

[1] Nozdrzykowski, K., Grządziel, Z., Kostrzewa, W. (2017). *Modelling and simulation tests of crankshaft deformations.* Machine Dynamics Research, 2017, No. 3, vol. 41, pp. 62-69.

[2] Nozdrzykowski, K. (2017). *Analysis and measurement of deformation of multipoint – supported crankshafts,* Machine Dynamics Research, 2017, No. 1, vol. 41, p. 65-76.

[3] Sun, J., Wang, J., Gui, C. (2010). *Whole crankshaft beam-element, finite-element method for calculating crankshaft deformation and bearing load of an engine.* Proceedings of the institution of mechanical engineers part journal of engineering tribology, 2010, vol. 224, pp. 299-303.

[4] Król, K., Wikło, M., Olejarczyk, K., Kołodziejczyk, K., Siemiątkowski, Z., Żurowski, W., Rucki, M. (2017). *Residual stress assessment in the marine diesel engine crankshaft* 12V38 type. Journal of KONES Powertrain and Transport, 2017, Vol. 24, No. 2, pp.117-123.

[5] Nozdrzykowski, K. (2017). *Adjustment and analysis of forces in a flexible crankshaft support system*, Journal of Machine Construction and Maintenance. 2017, No. 4, pp. 63-70.

[6] Nozdrzykowski, K. (2015). *Prevention of elastic strains in flexible large size machine parts with the use of elastic support*, Machine Dynamics Research. 2015, No.2, vol.39, pp. 111-122.

[7] Leigh, J. R. (2006). Applied Digital Control: *Theory, Design and Implementation*. Dover Publications, 2006.

[8] B&R Help tutorial to Automation Studio, 2018.

[9] Dorf, R.C., Bishop, R.H. (2017). *Modern control systems*. Pearson Education Limited, London, 2017.

Streszczenie

Monografia MATERIALS, TECHNOLOGIES, CONSTRUCTIONS ”Construction and design“ dotyczy ważnego obszaru z zakresu konstruowania i projektowania elementów i urządzeń przemysłowych. Składa się z czterech rozdziałów. Pierwszy rozdział dotyczy badań nad eliminacją zjawiska drań skrętnych wału korbowego w wielocylindrowych silnikach spalinowych. Autorzy pracy, na podstawie teorii smarowania elementów wirujących, zaproponowali nowy model matematyczny, opisujący zjawiska zachodzące wewnątrz tłumika drgań skrętnych. Na podstawie danych rzeczywistych przeprowadzono analizę numeryczną. Rozdział drugi dotyczy koncepcyjno-obliczeniowej analizy silnika turbinowego w aspekcie poprawy jego wydajności. Analizę numeryczną wykonano z zastosowaniem programu ANSYS Fluent. Wykazano, że wydajność silnika turbinowego można zwiększyć poprzez zastosowanie innowacyjnej koncepcji systemu synchronizacji zaworów. Rozdział trzeci przedstawia problematykę przetwarzania bardzo dużych zbiorów danych pomiarowych. Autor zaproponował podział zbioru na podzbiory zwane klastrami, zaproponował metodę potencjału do zlokalizowania ich środków, powiązał je ze statystyką i prawdopodobieństwem oraz zaprezentował wyniki implementacji tej metody. Rozdział czwarty przedstawia oryginalne, innowacyjne rozwiązanie pomiarowe, przeznaczone do długich, wykorbionych wałów. System ten umożliwia analizę i pomiar odkształceń wału korbowego w trakcie symulowanych obciążeń.

Abstract

The monograph MATERIALS, TECHNOLOGIES, CONSTRUCTIONS "Construction and design" deals with an important area of construction and design of elements and industrial equipment. It consists of four chapters. The first chapter concerns research on the elimination of the torsional vibration of crankshafts in multi-cylinder internal combustion engines. The authors of the paper, on the basis of the theory of lubrication of rotating elements, proposed a new mathematical model, describing the phenomena occurring inside the torsional vibration viscous damper. On the basis of actual data, a numerical analysis was carried out. The second chapter concerns the conceptual and computational analysis of the turbine engine in the aspect of improving its efficiency. The numerical analysis was performed with the use of ANSYS Fluent software. It was shown that turbine engine efficiency can be increased by using an innovative concept of the valve synchronization system. The third chapter presents the problems of processing very large sets of measurement data. The author proposed to divide the set into sub-sets called clusters, proposed a method of potential to locate their resources, linked them with statistics and probability and presented the results of the implementation of this method. Chapter four presents an original, innovative measurement solution for long, cranked shafts. This system enables the analysis and measurement of crankshaft deformations during simulated loads.